Combined Zircon, Molybdenite, and Cassiterite Geochronology and Cassiterite Geochemistry of the Kuntabin Tin-Tungsten Deposit in Myanmar

Wei Mao,[1] Hong Zhong,[1,2,†] Jiehua Yang,[1,†] Yanwen Tang,[1] Liang Liu,[1] Yazhou Fu,[1] Xingchun Zhang,[1] Kyaing Sein,[3] Soe Myint Aung,[3] Jie Li,[4] and Le Zhang[4]

[1]*State Key Laboratory of Ore Deposit Geochemistry, Institute of Geochemistry, Chinese Academy of Sciences, Guiyang 550081, China*

[2]*University of Chinese Academy of Sciences, Beijing 100049, China*

[3]*Myanmar Geosciences Society, Yangon 11041, Myanmar*

[4]*State Key Laboratory of Isotope Geochemistry, Guangzhou Institute of Geochemistry, Chinese Academy of Sciences, Guangzhou 510640, China*

Abstract

The Kuntabin Sn-W deposit, located in southern Myanmar, is characterized by abundant greisen-type and quartz vein-type cassiterite and wolframite mineralization. We have conducted multiple geochronological methods and isotope and trace element analyses to reveal the age and evolution of the Kuntabin magmatic-hydrothermal system.

Zircon U-Pb dating of the two-mica granite yielded a weighted mean $^{206}Pb/^{238}U$ age of 90.1 ± 0.7 Ma. Cassiterite U-Pb dating provided a lower intercept age of 88.1 ± 1.9 Ma in the Tera-Wasserburg U-Pb concordia diagram. Molybdenite Re-Os dating returned a weighted mean model age of 87.7 ± 0.5 Ma and an isochron age of 88.7 ± 2.7 Ma. These ages indicate a genetic relationship between granite and Sn-W mineralization in the Kuntabin deposit and record the earliest magmatism and Sn-W mineralization in the Sibumasu and Tengchong terranes related to subduction of the Neo-Tethys oceanic slab. Three generations of cassiterite have been identified with distinctive cathodoluminescence textures and trace element patterns, indicating the episodic input of ore-forming fluids and distinctive changes in the physical-chemical conditions of the Kuntabin magmatic-hydrothermal system. Sudden changes of fluid pressure, temperature, pH, etc., may have facilitated the deposition of Sn and W. Rhenium contents of molybdenite from the Kuntabin deposit and many other Sn-W deposits in Myanmar are characteristically low compared to porphyry Cu-Mo-(Au) deposits worldwide. In combination with zircon Hf isotope signatures, we infer that granites associated with Sn-W deposits in Myanmar were predominantly derived by melting of ancient continental crust and contain minimal mantle contribution.

Subduction of the Neo-Tethys oceanic slab from west of the West Burma terrane reached beneath the Sibumasu terrane and led to magmatism and Sn-W mineralization at ~90 Ma when the Kuntabin deposit was formed. The Paleoproterozoic Sibumasu crust was activated during the subduction-related magmatism to form predominantly crust derived melts. After a high degree of fractional crystallization and fluid exsolution, physical-chemical changes of the hydrothermal fluid resulted in Sn and W precipitation to form the Kuntabin Sn-W deposit.

Introduction

The Southeast Asian tin belt is the most important Sn-producing province in the world, historically accounting for ~54% of the world's tin production (Schwartz et al., 1995). It is a ~2,800-km-long belt that extends from Myanmar and Thailand to Peninsular Malaysia and the Indonesian tin islands (Campbell, 1920; Penzer, 1922; Clegg, 1944a, b; Mitchell, 1977, 1979; Schwartz et al., 1995; Searle et al., 2012; Gardiner et al., 2014, 2015a, 2016a; Zaw et al., 2017; Zhang et al., 2019). Myanmar, as an important component of the Western tin belt, was a significant tin and tungsten producer before World War II but experienced considerable depression during the past 60 years (Gardiner et al., 2014, 2015b). Numerous primary and placer tin deposits in Myanmar remained largely untapped for a long period of time owing to the country's political isolation (Gardiner et al., 2014, 2015b; Mitchell, 2018). However, Myanmar tin production increased sharply in recent times to account for ~10% of the world's production in 2014, making it the third global supplier after China and Indonesia (Kettle et al., 2014, 2015). Most of the exported tin concentrates were from the newly discovered mines at Man Makhsan in the Wa State (22°16' N, 99°02' E), which is only ~20 km from the China-Myanmar border (Htun et al., 2017; Mitchell, 2018). The political and economic opening of Myanmar is providing a good opportunity to have a deep insight into the Sn-W mineralization and related magmatism in Myanmar and in the Southeast Asian tin belt.

Zircon is a significant refractory accessory mineral that has been extensively used for dating the ages of magmatic rocks owing to its high concentrations of U and low contents of Pb (Mattinson, 1987; Hanchar and Hoskin, 2003). In addition, it may contain up to percent levels of Hf, which records the source of the magma with its isotopic signature (Kinny and Maas, 2003). As a major repository of Re, molybdenite is an ideal mineral for Re-Os geochronology (Stein et al., 2001). The method can provide the age of mineralization and is resistant to later-stage overprint (Stein et al., 2003; Selby and Creaser, 2004). The amount of Re in molybdenite typically ranges from parts per billion to a few thousand parts per million and may occasionally exceed 1 wt % (Mao et al., 1999; Berzina et al., 2005; Voudouris et al., 2009; Rathkopf et al.,

†Corresponding authors: e-mails, zhonghong@vip.gyig.ac.cn, yangjiehua@mail.gyig.ac.cn

603

2017). The mechanism controlling the content of Re in molybdenite is still ambiguous (Stein et al., 2001; Berzina et al., 2005; Voudouris et al., 2009). The recently developed in situ cassiterite U-Pb dating leads directly to mineralization age of the predominant ore mineral cassiterite in Sn deposits (Gulson and Jones, 1992; Yuan et al., 2008, 2011; Li, C.Y., et al., 2016; Zhang et al., 2017a, b; Cheng et al., 2019). Cassiterite (SnO_2) is a member of the rutile group metal oxides with a tetragonal lattice structure (Farmer et al., 1991). The refractory nature of cassiterite makes it resistant to post-ore hydrothermal overprint and weathering. The ionic radius of Pb^{2+} is too large to substitute the octahedrally coordinated tin, but the smaller U^{4+} is preferred by the quadrivalent-loving cassiterite (Gulson and Jones, 1992; Yuan et al., 2008; Li, C.Y., et al., 2016; Cheng et al., 2019); therefore, cassiterite may contain substantial amounts of U but trivial amounts of Pb and may remain closed for the U-Pb system. Moreover, a group of trace elements, including Al, Ti, Fe, Zr, Nb, In, Ta, W, Mn, and Sc, can be included into the cassiterite crystal lattice and may potentially be used to decipher the physical-chemical evolution of the ore-forming system (Möller et al., 1988; Farmer et al., 1991; Plimer et al., 1991; Murciego et al., 1997; Jiang et al., 2004; Parafiniuk et al., 2007; Neiva, 2008; Pavlova et al., 2015; Zhang et al., 2017b; Cheng et al., 2019).

The Kuntabin Sn-W deposit is an important tin and tungsten producer in southern Myanmar. This study aims at dating the formation ages and deciphering the evolution of the granite-related Kuntabin Sn-W deposit by the combined methods of zircon and cassiterite cathodoluminescence (CL), laser ablation-inductively coupled plasma-mass spectrometry (LA-ICP-MS) U-Pb dating, isotopic and trace element analyses, and molybdenite Re-Os dating. Our study is a major contribution to understanding the genetic relationship between the two-mica granites and cassiterite mineralization and the physical-chemical evolution of the hydrothermal system.

Geologic Setting

Regional geologic setting

Southeast Asia is composed of a complex collage of continental blocks that were successively derived from the margin of eastern Gondwana and then assembled by closure of successive Tethyan oceans and back-arc basins (Fig. 1A; Hutchison, 1975, 1977, 1983, 1994; Mitchell, 1977, 1981, 1986, 2018; Hutchison and Taylor, 1978; Beckinsale, 1979; Metcalfe, 1984, 1996, 2009, 2011, 2013; Cobbing et al., 1986; Searle et al., 2012; Zaw et al., 2014, 2017; Hou and Zhang, 2015; Liu et al., 2016a; Lin et al., 2019; Zhang et al., 2019). The Sibumasu block, together with the Tengchong, Baoshan, Qiangtang, and Lhasa blocks, was separated from Gondwana as the eastern part of the Cimmerian continental strip in the early Permian (Sengor, 1979, 1984, 1987; Searle et al., 2007). The term Sibumasu (Si = Sino and Siam, bu = Burma, ma = Malaya, su = Sumatra) refers to the elongate Gondwana-derived block characterized by late Paleozoic Gondwana biotas and late Carboniferous-early Permian glacial-marine diamictites (MetCalfe, 1984). The Baoshan terrane distributed in west Yunnan and the Sibumasu terrane either are the same terrane or were assembled together during or before the Triassic (MetCalfe, 1996, 2013; Gardiner et al., 2018), so Sibumasu

used here and after includes its north extension in Yunnan. The Tengchong terrane, hosted in north Myanmar and west Yunnan, is bounded to the west of the Sibumasu terrane by the Gaoligong shear zone (Fig. 1; Wopfner, 1996; Wang et al., 2014; Li, D.P., et al., 2016).

Based on the distinct mineralogical, geochemical, and geochronological affinities, the extensive distribution of granites in the Southeast Asian tin belt has been classified into three granite provinces since the 1970s (Fig. 1B; Hutchison, 1977, 1983; Mitchell, 1977, 1979, 1986, 1993; Hutchison and Taylor, 1978; Beckinsale, 1979; Cobbing et al., 1986, 1992; Leh-mann and Mahawat, 1989; Zaw, 1990; Charusiri et al., 1993; Schwartz et al., 1995; Searle et al., 2012). The Eastern granite province consists predominantly of I-type granites mainly distributed in eastern Malaysia, central-eastern Thailand, and northern Laos. This zone consists of the Lincang-Sukhothai-Chansaburi arc terrane and is bounded by the Jinghong-Nan-Uttaradit suture zone and a cryptic suture in the offshore of East Malay Peninsula to the east, and by the Changning-Menglian, Inthanon, and Bentong-Raub suture zones to the west (Charusiri et al., 1993; MetCalfe, 1996, 2011, 2013; Sone and Metcalfe, 2008; Wang et al., 2016). The Eastern province formed during the eastward subduction of the Paleo-Tethys from the Permian to Late Triassic (Charusiri et al., 1993; Cumming et al., 2008; Metcalfe, 2011; Searle et al., 2012; Salam et al., 2014; Fanka et al., 2018). Closure and suturing of the Paleo-Tethys Ocean occurred similarly from north Thailand and Myanmar to Peninsular Malaysia along the Changning-Menglian-Inthanon-Bentong-Raub suture zone at ~230 Ma (Ng et al., 2015a, b). Tin mineralization in the Eastern province is mainly hosted in east Malaysia and the Indonesian tin islands, while granites in other areas of the Eastern province either are barren (Lehmann and Mahawat, 1989; Schwartz et al., 1995) or host only minor mineralized occurences (Wang et al., 2014).

The Main Range (Central) granite province consists predominantly of S-type granites that mainly crop out in western Malaysia, western Thailand, eastern Myanmar, and western Yunnan. This zone mainly lies in the eastern part of the Sibumasu terrane and is bounded by the Mae Yuam fault and the Khlong Marui fault in the west (Fig. 1B; Mitchell, 1977, 1986; Cobbing et al., 1986; Charusiri et al., 1993; Schwartz et al., 1995). The Main Range granites formed in a limited time span of 227 to 201 Ma in a postcollisional crustal thickening setting within the Sibumasu block after the closure of the Paleo-Tethys Ocean (Beckinsale, 1979; Manning, 1986; Lehmann and Mahawat, 1989; Searle et al., 2007; Ng et al., 2015a, b; Wang et al., 2016). Medium-sized Sn-W deposits have been reported in the Changing-Menglian Sn belt in west Yunnan and in north Thailand (Khositanont, 1990; Wang et al., 2014). In contrast, west Peninsular Malaysia is one of the world's richest Sn provinces, hosting significant Sn-producing regions like Kinta Valley and Klang Valley (Yeap, 1993).

The Western granite province, usually assigned as a mixture of I- and S-type granites of mainly Cretaceous to Cenozoic ages, runs through peninsular Thailand and Myanmar, extending to west Yunnan, China. This zone is mainly distributed in western part of the Sibumasu terrane and is bounded by the Sagaing fault and the Myitkyina suture zone in the west (Fig. 1B; Mitchell, 1977, 1979, 1986, 1993; Hutchison and Taylor,
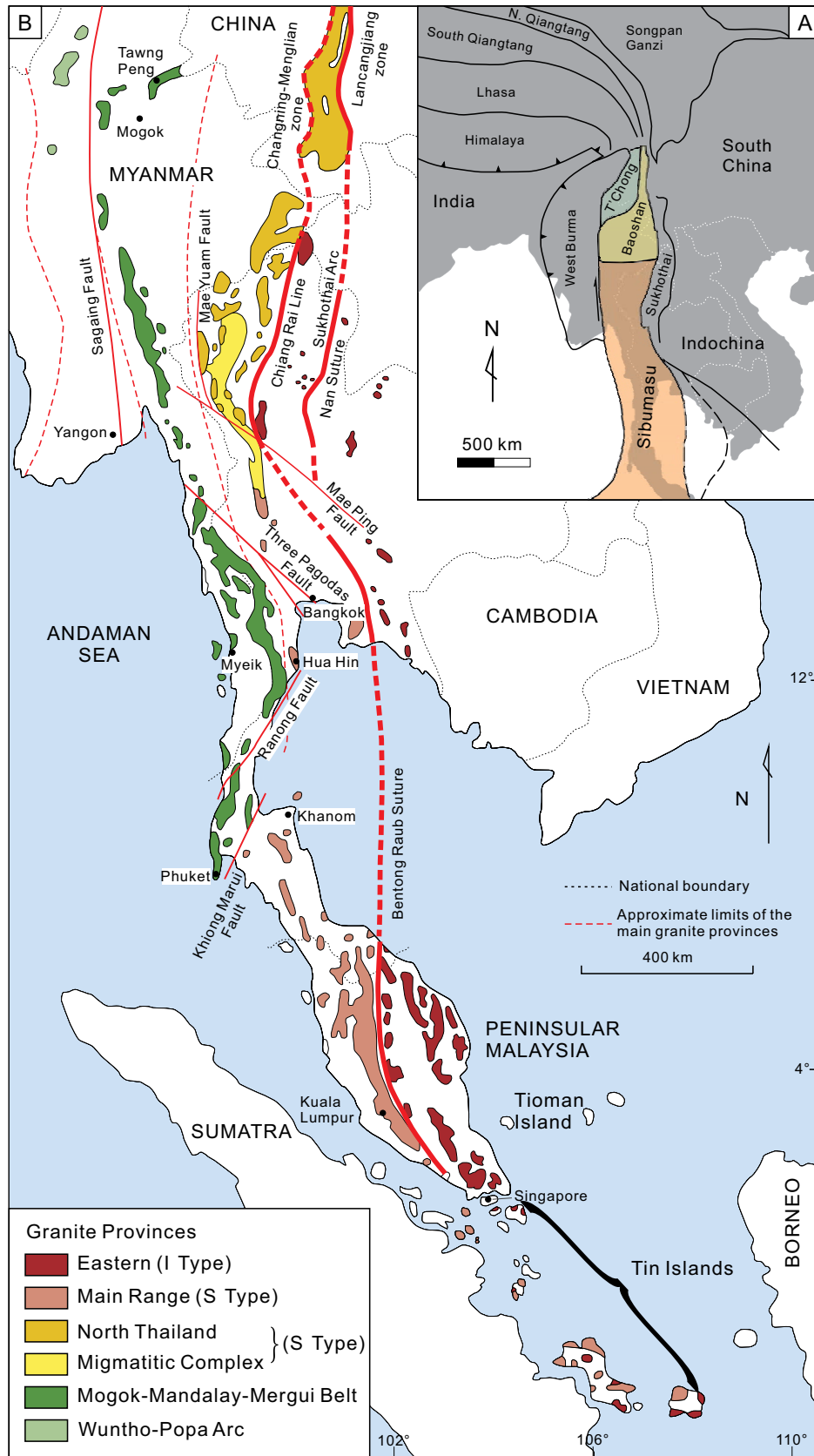
Fig. 1. (A) Tectonic subdivision of Southeast Asia. Modified after Gardiner et al. (2018). (B) Simplified map showing the granite belts in Southeast Asia. Modified after Cobbing et al. (1986), Charusiri et al. (1993), Sone and Metcalfe (2008), and Gardiner et al. (2016a, b).

1978; Beckinsale, 1979; Cobbing et al., 1986, 1992; Lehmann and Mahawat, 1989; Zaw, 1990; Mitchell et al., 2012; Searle et al., 2012; Ng et al., 2015a, b). The Western province experienced a more complicated tectonic evolution that generated episodic magmatic activities during the successive subduction of Tethys oceans and accretion of the Tengchong, West Burma, and Indo-Burma terranes since the Jurassic (Mitchell, 1977, 1979, 1981, 2018; Bender, 1983; Zaw, 1984; Barley et al., 2003; Searle et al., 2007; Gardiner et al., 2015a, b, 2016a, b, 2018; Li, J.X., et al., 2018; Lin et al., 2019). Significant Sn-W mineralization occurred in the Western province and formed many world-class deposits (Clegg, 1944a, b; Mitchell, 1977, 1981, 1986; Gardiner et al., 2015a, b, 2016a, b; Htun et al., 2017).

The Popa-Loimye magmatic arc (Wuntho-Popa arc), hosted in the West Burma terrane, is bounded by the Sagaing fault in the east and the Kalaymyo (Kalemyo) suture in the west (Figs. 1, 2; Bender, 1983; Gardiner et al., 2014, 2016a, b; Mitchell et al., 2015; Li, J.X., et al., 2018; Lin et al., 2019). Exposure of intrusive and volcanic rocks in this region is discontinuous owing to the wide occurrences of sedimentary cover (Myanmar Geosciences Society, 2014). Granite in this arc is dominantly I type, related to the subduction of the Neo-Tethys Ocean (Gardiner et al., 2014, 2016a, b; Li, J.X., et al., 2018; Lin et al., 2019). In contrast to the significant Sn-W mineralization in the above granite provinces, the Popa-Loimye magmatic arc hosts some porphyry Cu-Au and epithermal Au deposits, including the Shangalon porphyry Cu-Au deposit (Gardiner et al., 2016a, b, 2018; Zaw, 2017) and the Monywa high-sulfidation Cu deposit (Mitchell et al., 2011).

The Western tin belt

The Western tin belt refers to Sn-W deposits and related granites distributed in the slate belt and the Shan scarps of Myanmar and southwest Thailand and extending north into west Yunnan in China (Fig. 1; Mitchell, 1977, 2018; Schwartz et al., 1995; Gardiner et al., 2016a, b). Explorations of the Sn-W mineralization in Myanmar and adjacent regions have been conducted from over a century ago (Campbell, 1920; Penzer, 1922; Brown and Heron, 1923; Chhibber, 1934; Clegg, 1944a, b). Scientific studies of Sn-W deposits in the Western tin belt considering the geologic settings, magma origin, ages of mineralization, and ore-forming mechanisms have been conducted by many researchers (Chhibber, 1934; Mitchell, 1977, 1981, 1986; Beckinsale, 1979; Bender, 1983; Shawe, 1984; Lehmann and Mahawat, 1989; Charusiri et al., 1993; Myint, 1994; Pollard et al., 1995; Schwartz et al., 1995; Win and Myint, 1998; Xu et al., 2012; Chen et al., 2014; Gardiner et al., 2014a, b, 2015a, b, 2016a, b; Wang et al., 2014; Zaw, 2017; Li, J.X., et al., 2018). Most of the tin-related granites in the Western tin belt are peraluminous biotite, biotite-muscovite, or less commonly muscovite-tourmaline granites (Charusiri et al., 1993; Gardiner et al., 2016a, b; Htun et al., 2017; Mitchell, 2018). Approximately 80% of Sn production in Thailand and nearly all the Sn production from Myanmar were from the Western tin belt (Schwartz et al., 1995). Magmatism in the Western tin belt can be classified into three episodes (Gardiner et al., 2014a, b, 2015a, b, 2016a, b; Wang et al., 2014; Li, J.X., et al., 2018). The Early to Mid-Jurassic granites are limitedly distributed in the northern part of the Sibumasu terrane and are generally barren. The Early Cretaceous gra-

nitic magmatism is mainly hosted in the Tengchong terrane and northern part of the Sibumasu terrane, and related Sn-W mineralization includes the Tieyaoshan and Jiaojiguan Sn deposits in Yunnan and the Dapingba Mo-W deposit in northern Myanmar (Chen et al., 2014; Li, J.X., et al., 2018). The Late Cretaceous to Eocene granitic magmatism is distributed all
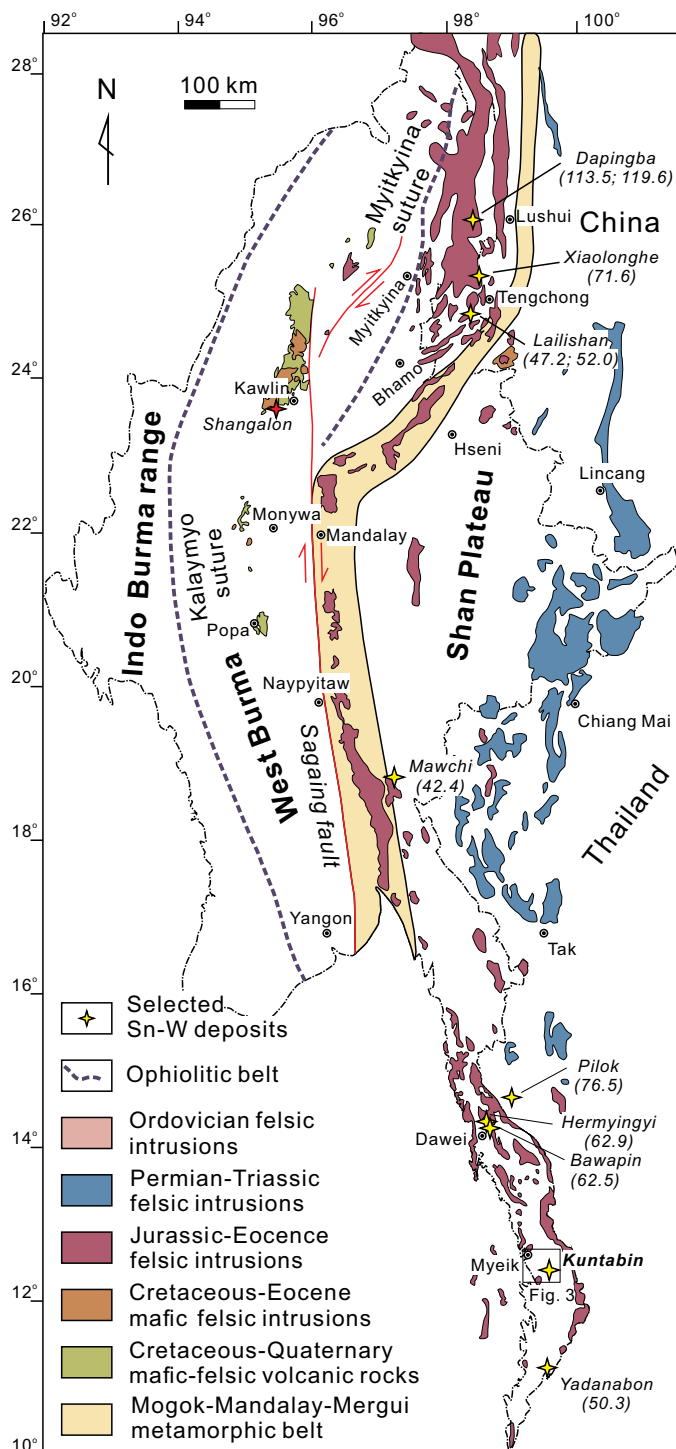

Fig. 2. Simplified geologic map of Myanmar with the distribution of selected Sn-W deposits. Modified after J.X. Li et al. (2018). Ages of Sn-W mineralization are from Linnen and Williams-Jones (1995), Chen et al. (2014, 2015), Gardiner et al. (2016a, b, 2018), and J.X. Li et al. (2018).

over the Western tin belt, with abundant important Sn-W deposits, including the Xiaolonghe and Lailishan Sn-W deposits in west Yunnan, the Mawchi deposit in the Kayah district and the Hermyingyi deposit in the Dawei district of Myanmar, the Pilok deposit in west Thailand, and many deposits from the Phuket district in southwest Thailand (Fig. 2). Oligocene and Miocene granites occur in the Shan scarps and the Mogok metamorphic belt in Myanmar; however, none of them are related to Sn-W mineralization (Barley et al., 2003; Searle et al., 2007; Mitchell et al., 2012; Gardiner et al., 2016a, b; Crow and Zaw, 2017).

Ore deposit geology

The Mergui (Myeik) district in southern Myanmar is characterized by numerous small mines producing tin and only minor tungsten (Fig. 2; Penzer, 1922; Clegg, 1944a, b; Mitchell, 1977, 1981, 1986, 2018; Gardiner et al., 2015a, b, 2016a, b; Htun et al., 2017). In 1939, the Mergui district produced around 1,027 tons (t) of cassiterite and only 343 t of wolframite concentrates (Clegg, 1944a, b). The high ratio of tin to tungsten in the Mergui district, in comparison to other regions in Myanmar, was partly attributed to the abundance of alluvial deposits and few lode deposits (Mitchell, 2018). Clegg

(1944a) listed 275 mines in the Mergui district, and 197 of them were still in production in 1939, including 161 mines producing only cassiterite, 32 mines producing cassiterite and wolframite, and four mines producing only wolframite.

The Tagu area, located ~45 km to the southeast of the Myeik city and ~15 km to the north-northwest of Tanintharyi town, hosts several important Sn-W deposits (Fig. 3; Clegg, 1944a, b; Mitchell, 2018). Abundant Mesozoic-Cenozoic granites crop out in the Tanintharyi division. Sedimentary rocks of the Tanintharyi region include the Quaternary alluvium; the late Miocene to Pliocene Irrawaddy Group of fluviatile, unconsolidated, poorly to thinly bedded sandstones; the Jurassic red beds equivalent to the Loi-an Group and Namyau Group; and the upper Paleozoic Mergui group of mudstones or argillites (Mitchell, 1992; Myanmar Geoscience Society, 2014). The Mergui Group was named after the Mergui series described by Oldham (1856) in the Tanintharyi region. The sedimentary rocks in the Mergui Group were locally metamorphosed to mica schists and interbedded thinner sandstones or quartzites, with minor conglomerates and rare limestones. The most distinctive lithology of the Mergui Group is pebbly mudstone and pebbly wacke or diamictite (Mitchell, 2018).

Three Sn-W deposits, including the Tagu No. 1, Tagu No. 2,
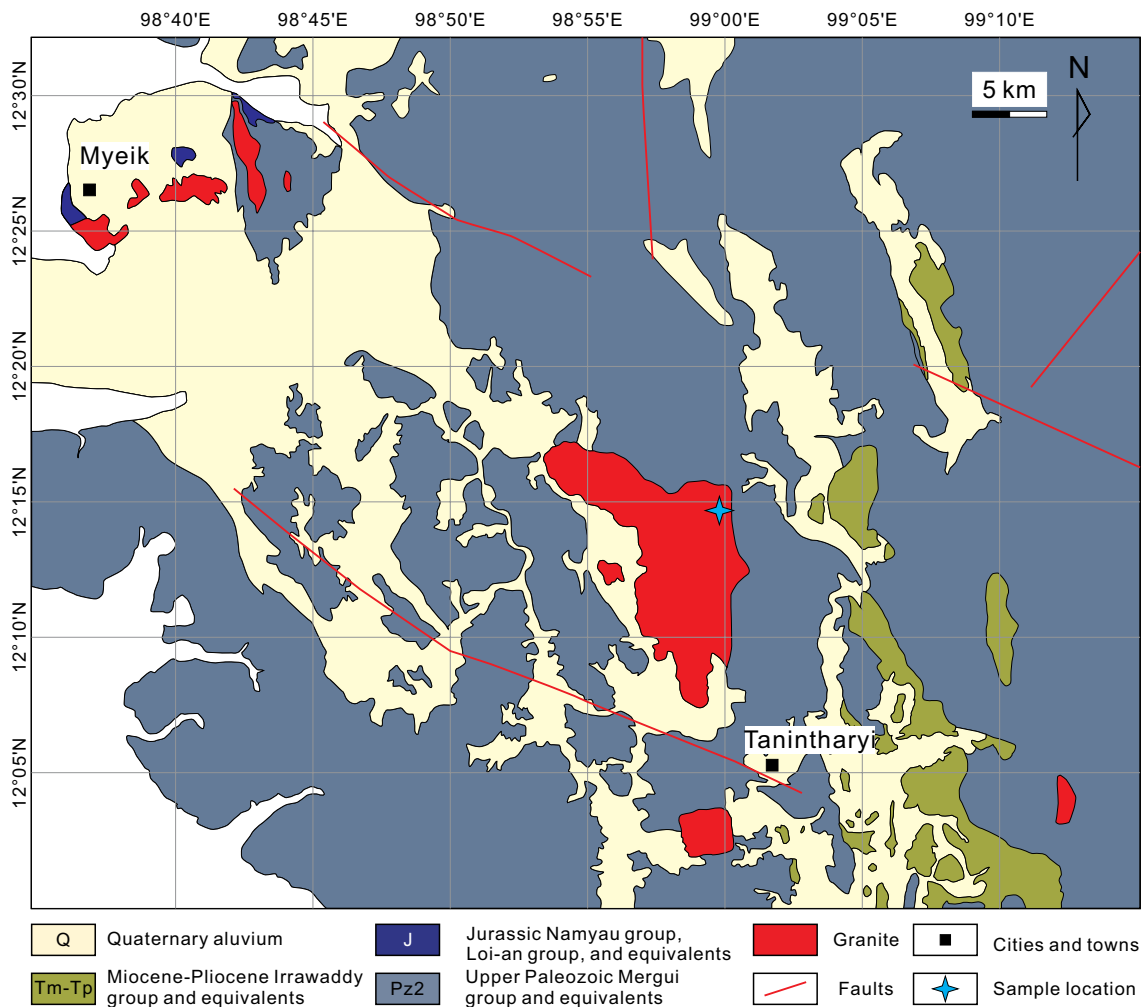

Fig. 3. Geologic map of the Myeik district, Tanintharyi division.

and the Kuntabin Sn-W deposits, lie on the flanks of the Letha Taung (Letha Mountain) in the Tagu area (Clegg, 1944a). Tin and tungsten ores in these deposits occur as lodes in the uphills, eluvium in the slopes, and alluvium in the valley bottoms. Around 25 t of cassiterite and 98 t of wolframite concentrates have been produced since 1939 in the Tagu area. In the Tagu No. 1 deposit, southeast of the Letha Taung, at least 150 quartz veins are hosted mainly in schist and minimally in granite below. Vein width ranges from millimeters to ~80 cm, dipping steeply southeast. Ore grade generally decreases in veins from the schist down into the granite. Thickness ranges from ~2.5 to ~10 m for the eluvial mines on the hills and is around 7.5 m for the alluvial mines in the valleys (Clegg, 1944a).

The Kuntabin Sn-W deposit (12.24° N, 98.99° E) lies on the northeast flanks of the Letha Taung. The ore-forming granite in the Kuntabin Sn-W deposit is medium- to coarse-grained two-mica granite (Fig. 4A). It consists of ~30% quartz, ~50% feldspar, ~10% biotite, and ~10% muscovite, with rutile, apatite, and zircon occurring as accessory minerals. Biotite is partly altered to chlorite, and K-feldspar is partly altered to clay minerals (Fig. 4G, H). Intensive greisenization occurred where hydrothermal fluid flowed through the fractures in granite to form wide quartz veins and greisen-type mineralization. The two-mica granite on
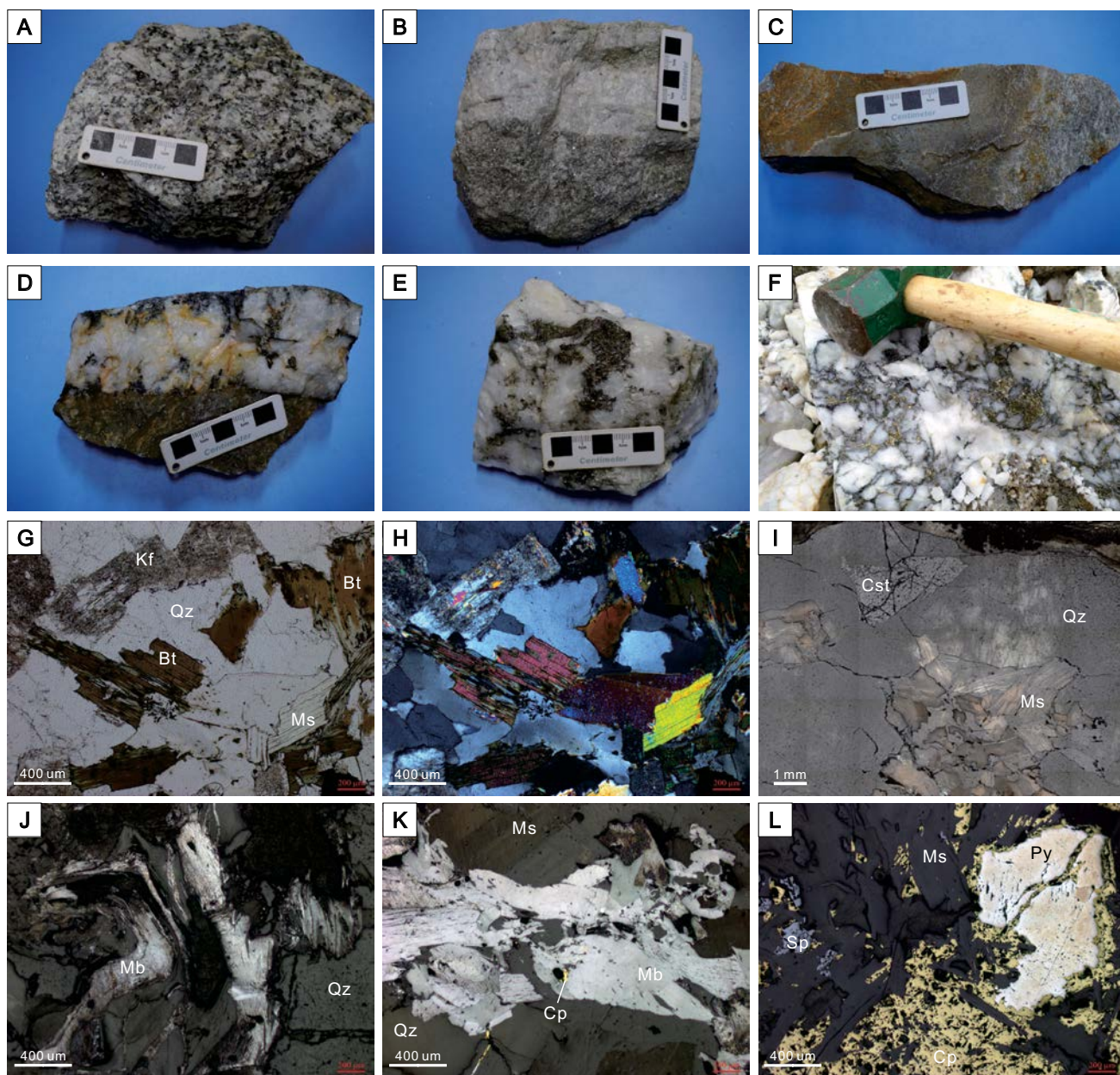

Fig. 4. Rocks and quartz-bearing veins from the Kuntabin Sn-W deposit. (A) Least altered two-mica granite. (B) Greisen and quartz-bearing vein. (C) The Megui Group schists. (D-F) Quartz-cassiterite-sulfide vein hosted in the Mergui Group. (G, H) Plane-polarized and cross-polarized images of the two-mica granite. (I) Reflected-light image of a quartz-bearing vein. (J-L) Reflected-light images of sulfides. Abbreviations: Bt = biotite, Cp = chalcopyrite, Cst = cassiterite, Kf = K-feldspar, Mb = molybdenite, Ms = muscovite, Py = pyrite, Qz = quartz, Sp = sphalerite.

both sides of the quartz veins is altered to muscovite and quartz during greisenization (Fig. 4B). Magnetite, molybdenite, and chalcopyrite are observed where hydrothermal alteration occurred. Abundant quartz veins having widths ranging from several millimeters to over 40 cm and dipping steeply southwest are hosted in the Kuntabin deposit. The majority of the Sn and W ores are hosted in schist of the Mergui Group as quartz-vein type mineralization. A small proportion of the Sn and W ore is hosted in the altered granite as greisen-type mineralization. Ore minerals are predominantly cassiterite and wolframite, but minor molybdenite, chalcopyrite, pyrite, arsenopyrite, and bismuthinite can be identified (Fig. 4I-L). Sulfide minerals are more abundant in quartz veins hosted in the schist than in the granite. Cassiterite and wolframite typically show euhedral to subhedral texture with sizes of up to 3 mm (Fig. 4I). Colors of cassiterite range from light brown to black, and colors of wolframite are black to brown. Sulfides generally postdate cassiterite and wolframite precipitation. Molybdenite is the earliest precipitated sulfide and is followed by the precipitation of pyrite and then chalcopyrite and sphalerite (Fig. 4J-L). The lode mines were worked during the dry seasons in adits and open cuts, and the eluvial and alluvial mines were worked by hand sluicing during the rainy seasons.

Analytical Methods

Zircons were separated from over 2 kg of the least altered two-mica granite from the Kuntabin Sn-W deposit by conventional methods, including crushing, concentration by hand washing, and magnetic and heavy liquid separation. The selected zircon grains were then purified after handpicking under a binocular microscope. A quartz-cassiterite-sulfide vein rich in cassiterite was crushed, hand washed, and purified under a binocular microscope to separate the cassiterite. Both zircon and cassiterite grains were mounted in epoxy blocks and polished for further analysis. Transmitted-light images, reflected-light images, and CL images of zircon and cassiterite were used to avoid the ablation of fluid and mineral inclusions during the LA-ICP-MS work. Molybdenite was separated from quartz-cassiterite-molybdenite veins and molybdenite-bearing greisen samples and crushed to 200 mesh.

Zircon and cassiterite CL

Scanning electron microscopy (SEM)-CL images of zircon and cassiterite were obtained at the Beijing Geoanalysis Co., Ltd. with a JEOL JSM6510 scanning electron microscope equipped with a Gatan CL detector. An acceleration voltage of 15 kV, a probe current of ~6 nA, and a magnification of ~250× were used for zircon. An acceleration voltage of 15 kV, a probe current of ~6 nA, and a magnification of ~100 to 200× were used for cassiterite.

Zircon and cassiterite LA-ICP-MS U-Pb dating and trace element analyses

Zircon and cassiterite LA-ICP-MS U-Pb dating and trace element analysis were conducted at the State Key Laboratory of Ore Deposit Geochemistry, Institute of Geochemistry, Chinese Academy of Sciences (SKLODG, IGCAS). The analytical system is composed of a GeoLas Pro 193-nm ArF excimer laser ablation system and an Agilent 7500× ICP-MS instrument. He-

lium was used as carrier gas and was mixed with argon via a T-connector before entering the ICP-MS. Zircon U-Pb analysis was carried out with a laser energy density of 5 J/cm², a repetition of 5 Hz, and a spot size of 32 μm. The zircon standard 91500 was used as external standard for zircon U-Pb dating and returned the weighted mean $^{206}Pb/^{238}U$ age of 1062.5 ± 7.1 Ma, which is identical to the recommended isotope dilution-thermal ionization mass spectrometry (ID-TIMS) age of 1062.4 ± 0.8 Ma (Wiedenbeck et al., 1995). The zircon standard Plešovice was analyzed as the unknown and returned the weighted mean $^{206}Pb/^{238}U$ age of 337.2 ± 2.3 Ma, which is identical to the recommended ID-TIMS age of 337.13 ± 0.37 Ma (Sláma et al., 2008). Cassiterite U-Pb and trace element analyses were conducted separately with a laser energy density of 8 J/cm², a repetition of 7 Hz, and a spot size of 60 μm. The cassiterite standard AY-4 was used as external standard for cassiterite U-Pb dating and returned the weighted mean $^{206}Pb/^{238}U$ age of 158.1 ± 1.6 Ma, which is identical to the recommended ID-TIMS age of 158.2 ± 0.4 Ma (Yuan et al., 2008). Standard reference material (NIST 612) was used for cassiterite trace element calculation using Sn as internal standard. Data reduction was carried out by the ICPMSDataCal program (Liu et al., 2008, 2010). Concordia diagrams and weighted mean age calculations were made using the Isoplot program (Ludwig, 2003).

Cassiterite electron microprobe analysis (EMPA) spot analysis and mapping

Spot analysis and X-ray mapping of cassiterite were carried out with a JXA8230 electron microprobe at the SKLODG, IGCAS. Elements including Sn, Al, Fe, In, Mn, Nb, Ta, Ti, U, and W were analyzed during spot analysis at the settings of 25-kV accelerating voltage, 10-nA beam current, and 10-μm beam size. Mapping was conducted at the settings of 25-kV accelerating voltage, 20-nA beam current, and 1-μm beam size.

Zircon Hf isotope analysis

In situ zircon Hf isotope analyses were conducted at the SKLODG, IGCAS. The analytical system is composed of a RESOlution S-155 193-nm excimer laser ablation and a Nu Plasma III multicollector (MC)-ICP-MS. A laser energy density of 6 J/cm², a repetition of 6 Hz, and a spot size of 60 μm were used for zircon Hf isotope analysis. Laser ablation spots for Hf isotopes were on the same zircon grains that were previously analyzed for U-Pb isotopes. Detailed analytical procedures can be found in Wu et al. (2006). The $\varepsilon_{Hf}(t)$ values were calculated relative to the chondritic reservoir, with the decay constant of $1.867 ± 0.00810^{-11}$ yr^{-1} (Scherer et al., 2001). The two-stage Hf model ages (T_{DM2}) were calculated assuming a mean $^{176}Lu/^{177}Hf$ value of 0.015 for the average continental crust (Griffin et al., 2002). Correction for isobaric interference of ^{176}Lu and ^{176}Yb on ^{176}Hf was conducted using $^{176}Yb/^{173}Yb = 0.7962$ and $^{176}Lu/^{175}Lu = 0.02655$ with an exponential-law mass bias correction assuming a $^{173}Yb/^{171}Yb$ ratio of 1.129197 (Vervoort et al., 2004). Zircon Penglai was used as the reference material, which has the weighted average $^{176}Yb/^{177}Hf$ ratio of 0.016272 ± 0.000027, comparable to zircon from the Kuntabin two-mica granite. Zircon Penglai returned the weighted mean $^{176}Hf/^{177}Hf$ results of 0.282907 ± 0.000013, identical to the recommended value of 0.282906 ± 0.000010 (Li, X.H., et al., 2010).

Molybdenite Re-Os dating

Molybdenite Re-Os dating was conducted at the State Key Laboratory of Isotope Geochemistry, Guangzhou Institute of Geochemistry, Chinese Academy of Sciences. Samples, to which the [185]Re spike and Os standard were added, were loaded in Carius tubes and digested with aqua regia at 200°C for over 24 h. After cooling of the solution, Os was separated from Re by CCl_4 extraction and purified by microdistillation. Rhenium was separated from the major matrix elements (e.g., Mo, W, and Fe) by solvent extraction with N-benzoyl-N-phenylhydroxylamine (BPHA) in chloroform solution (Du et al., 2004; Shinotsuka and Suzuki, 2007; Li, J., et al., 2010; Qi et al., 2010). The purified Re and Os were then analyzed by ICP-MS (Perkin-Elmer Elan 6000) equipped with a concentric glass nebulizer (Glass Expansion, Australia). Molybdenite reference material (GBW04436: JDC), with certified age of 139.6 ± 3.8 Ma (Du et al., 2004), was analyzed and yielded identical model ages of 140.5 ± 1.1 and 139.7 ± 1.0 Ma.

Results

Zircon U-Pb age and Hf isotopes

Zircons from the Kuntabin Sn-W deposit generally show euhedral crystal shape, with lengths ranging from ~100 to over 200 μm. Fluid and mineral inclusions were identified in many zircons and carefully avoided during laser ablation. Most of the zircons have clear oscillatory zonation CL textures, indicating that they are magmatic zircons (Fig. 5). The LA-ICP-MS results of zircon analysis are presented in Table 1. The error in individual analysis is at the 1σ level, and the weighted mean [206]Pb/[238]U age is at the 95% confidence level.

Thorium contents vary from 258 to 1,628 ppm, with an average of ~630 ppm. Uranium contents range from 496 to 5,790 ppm, with an average of ~2,125 ppm. The Th/U ratios lie between 0.07 and 1.43, with an average of ~0.45. All the analytical results cluster tightly on the concordia curve with an age of 90.0 ± 0.8 Ma (2σ; mean square of weighted deviates [MSWD] = 0.33) (Fig. 5). The analytical results yield a weighted mean [206]Pb/[238]U age of 90.1 ± 0.7 Ma (2σ; MSWD = 0.34). This age represents the crystallization age of the two-mica granite.

The analytical results of zircon Hf isotopes and related parameters are listed in Table 2. [176]Hf/[177]Hf values of 14 zircon grains range from 0.282266 to 0.282466, corresponding to $\varepsilon_{Hf}(t)$ values of –16.0 to –8.9, with an average of ~–12.6. The two-stage Hf model ages (T_{DM2}) vary from 2161 to 1712 Ma, with an average of ~1950 Ma.

Cassiterite CL textures

Cassiterite from the Kuntabin Sn-W deposit typically shows euhedral crystal shapes with size up to 3 mm in hand samples. After being crushed and separated, the cassiterite grains are usually broken into smaller pieces but may still preserve sharp grain boundaries (Fig. 6). At least three generations of cassiterite can be identified based on their distinctive intensity and textures in CL images.

Cassiterite-I (Cst-I): CL intensity of this generation of cassiterite is very low, so that Cst-I is generally homogeneous and black in CL images. However, oscillatory zones formed by alternating thin bands (<15 μm) with slightly different CL intensities can be identified (Fig. 6B, D). Most of the Cst-I grains are eroded to form a rounded core (Fig. 6A, E), brecciated and cemented by later-stage cassiterite (Fig. 6A), or fractured and overprinted by later-stage cassiterite mineralization (Fig. 6B).

Cassiterite-II (Cst-II): CL intensity of this generation of cassiterite is much higher compared to Cst-I, so Cst-II is typically bright in CL images with very clear and thin oscillatory zones parallel to the growth zones but may be locally black
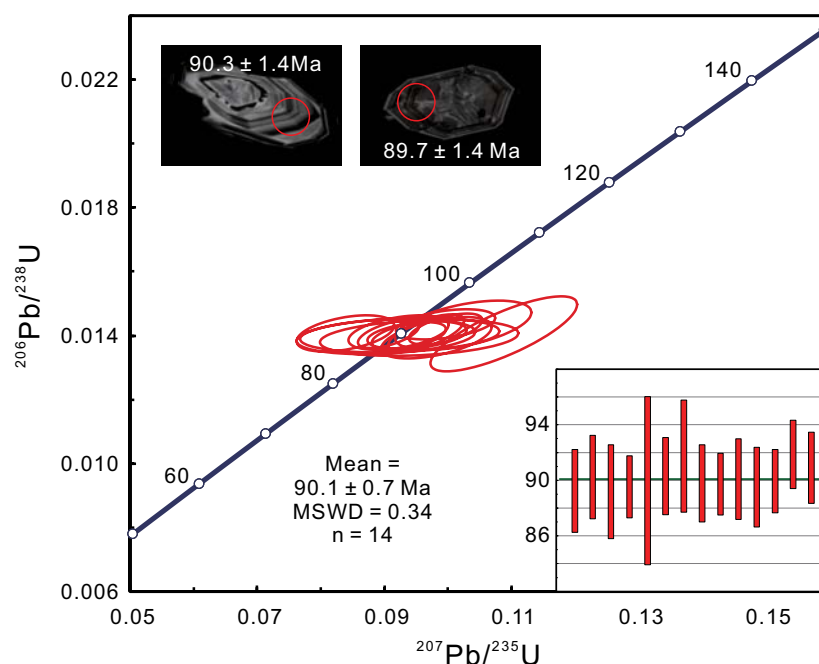

Fig. 5. Zircon CL images, U-Pb concordia, and weight mean age diagrams for the two-mica granite from the Kuntabin Sn-W deposit. Red circles are the laser ablation spots with the size of 32 μm in diameter. MSWD = mean square of weighted deviates.

Table 1. U-Pb Isotope Ratios and Ages of Zircon from the Kuntabin Sn-W Deposit

Spot	Th (ppm)	U (ppm)	Th/U	207Pb/206Pb Ratio	1σ	207Pb/235U Ratio	1σ	206Pb/238U Ratio	1σ	207Pb/235U Age (Ma)	1σ	206Pb/238U Age (Ma)	1σ
KTB-Zrn-1	412	496	0.83	0.0495	0.0033	0.0955	0.0064	0.0139	0.0002	92.6	5.9	89.2	1.5
KTB-Zrn-2	860	3,087	0.28	0.0497	0.0013	0.0965	0.0024	0.0141	0.0002	93.6	2.3	90.2	1.5
KTB-Zrn-3	460	1,054	0.44	0.0511	0.0019	0.0982	0.0036	0.0139	0.0003	95.1	3.3	89.2	1.7
KTB-Zrn-4	258	3,625	0.07	0.0484	0.0011	0.0938	0.0024	0.0140	0.0002	91.1	2.2	89.5	1.1
KTB-Zrn-5	357	707	0.51	0.0563	0.0020	0.1088	0.0047	0.0141	0.0005	104.9	4.3	89.9	3.0
KTB-Zrn-6	318	2,406	0.13	0.0472	0.0015	0.0922	0.0032	0.0141	0.0002	89.6	3.0	90.3	1.4
KTB-Zrn-7	357	895	0.40	0.0520	0.0022	0.1024	0.0044	0.0143	0.0003	99.0	4.0	91.7	2.0
KTB-Zrn-8	417	729	0.57	0.0480	0.0040	0.0925	0.0064	0.0140	0.0002	89.8	6.0	89.7	1.4
KTB-Zrn-9	379	1,876	0.20	0.0490	0.0016	0.0952	0.0032	0.0140	0.0002	92.3	3.0	89.7	1.1
KTB-Zrn-10	444	1,304	0.34	0.0431	0.0014	0.0839	0.0031	0.0141	0.0002	81.8	2.9	90.1	1.4
KTB-Zrn-11	779	543	1.43	0.0474	0.0032	0.0903	0.0058	0.0140	0.0002	87.7	5.4	89.5	1.4
KTB-Zrn-12	1,005	4,928	0.20	0.0468	0.0009	0.0907	0.0020	0.0140	0.0002	88.2	1.8	89.9	1.1
KTB-Zrn-13	1,628	2,307	0.71	0.0506	0.0019	0.0997	0.0032	0.0143	0.0002	96.5	2.9	91.8	1.2
KTB-Zrn-14	1,146	5,790	0.20	0.0509	0.0012	0.0996	0.0024	0.0142	0.0002	96.4	2.2	90.9	1.3

Table 2. Hf Isotope Signatures of Zircon from the Kuntabin Sn-W Deposit

| Spot	Age Ma	1σ	176Hf/177Hf Value	1σ	176Lu/177Hf Value	1σ	176Yb/177Hf Value	1σ	176Hf/177Hf initial Value	εHf(t) Value	2σ	TDM1 (Ma) Value	2σ	TDM2 (Ma) Value	2σ	fLu/Hf
KTB-Hf-1	90.1	0.7	0.282334	0.000010	0.000515	0.000003	0.019605	0.000130	0.282333	-13.6	0.3	1280	26	2008	42	-0.98
KTB-Hf-2	90.1	0.7	0.282359	0.000009	0.001657	0.000007	0.054977	0.000240	0.282356	-12.7	0.3	1283	26	1956	41	-0.95
KTB-Hf-3	90.1	0.7	0.282394	0.000010	0.000289	0.000009	0.009408	0.000240	0.282394	-11.4	0.4	1189	27	1872	45	-0.99
KTB-Hf-4	90.1	0.7	0.282354	0.000011	0.001102	0.000006	0.035550	0.000096	0.282353	-12.9	0.4	1271	31	1964	49	-0.97
KTB-Hf-5	90.1	0.7	0.282336	0.000010	0.000619	0.000003	0.020725	0.000110	0.282335	-13.5	0.4	1280	28	2003	45	-0.98
KTB-Hf-6	90.1	0.7	0.282466	0.000009	0.000090	0.000001	0.004166	0.000047	0.282466	-8.9	0.3	1085	25	1712	41	-1.00
KTB-Hf-7	90.1	0.7	0.282383	0.000009	0.000687	0.000004	0.023468	0.000170	0.282382	-11.8	0.3	1217	26	1899	42	-0.98
KTB-Hf-8	90.1	0.7	0.282389	0.000011	0.000756	0.000002	0.025064	0.000041	0.282388	-11.6	0.4	1211	31	1885	49	-0.98
KTB-Hf-9	90.1	0.7	0.282303	0.000010	0.000689	0.000002	0.025372	0.000073	0.282302	-14.7	0.3	1328	27	2077	44	-0.98
KTB-Hf-10	90.1	0.7	0.282266	0.000012	0.000951	0.000006	0.029050	0.000160	0.282264	-16.0	0.4	1390	33	2161	53	-0.97
KTB-Hf-11	90.1	0.7	0.282410	0.000011	0.000699	0.000004	0.023858	0.000081	0.282409	-10.9	0.4	1180	31	1839	49	-0.98
KTB-Hf-12	90.1	0.7	0.282376	0.000011	0.001471	0.000009	0.047500	0.000280	0.282374	-12.1	0.4	1252	31	1917	49	-0.96
KTB-Hf-13	90.1	0.7	0.282332	0.000011	0.001425	0.000006	0.047792	0.000320	0.282329	-13.7	0.4	1314	31	2016	49	-0.96
KTB-Hf-14	90.1	0.7	0.282341	0.000010	0.000855	0.000007	0.028637	0.000220	0.282339	-13.3	0.3	1282	27	1994	43	-0.97
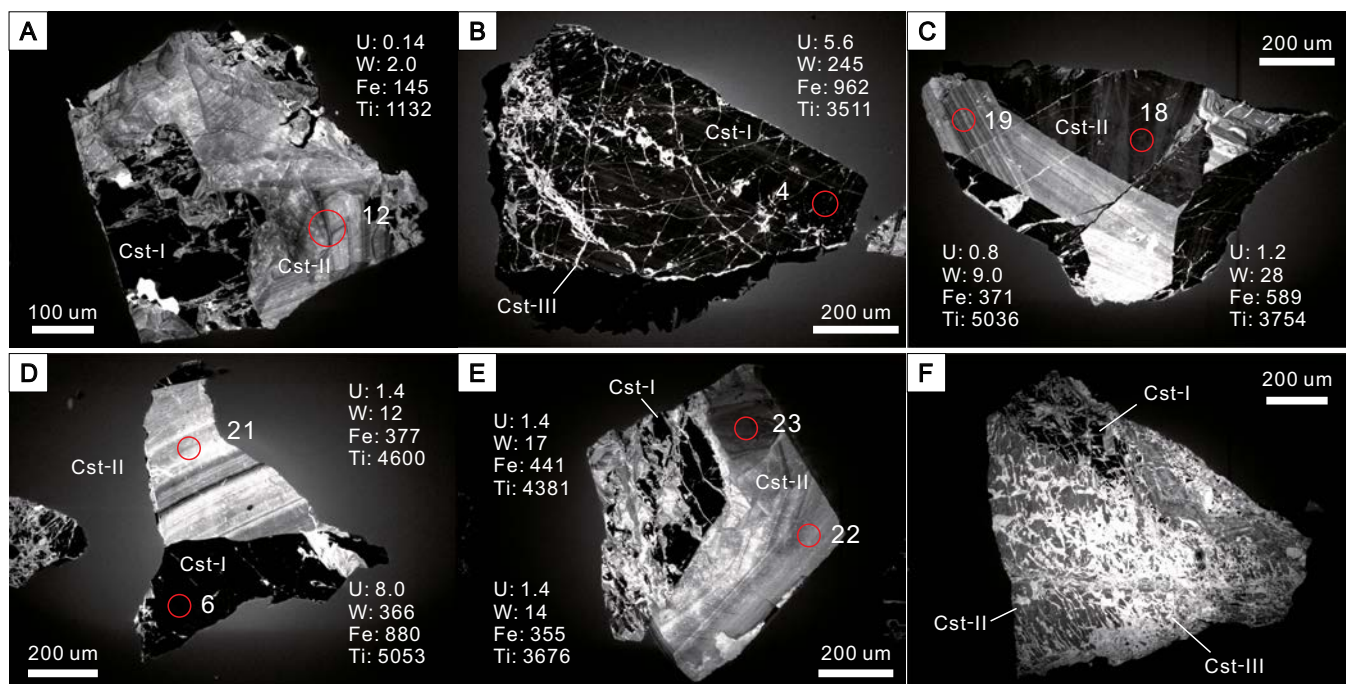
Fig. 6. Cassiterite CL images and trace element contents (in ppm). Red circles are the laser ablation spots for trace elements with the size of 60 μm in diameter.

in some crystal faces (Fig. 6C). Cst-II forms either individual crystals (Fig. 6C) or overgrowth on the preexisting Cst-I grains (Fig. 6A, E, F). Many of the Cst-II grains are fractured and refilled with later-stage cassiterite (Fig. 6C, F).

Cassiterite-III (Cst-III): CL intensity of this generation of cassiterite is higher than previous cassiterite. Cst-III grains are commonly white and homogeneous in CL images (Fig. 6B, F) but may display some growth zones locally. Cst-III consistently fills fractures in the preexisting cassiterite grains (Fig.

6B-D, F). Width of the Cst-III is commonly smaller than 30 μm, therefore cannot be used for LA-ICP-MS U-Pb and trace element analysis in this study.

Cassiterite trace element geochemistry

Thirteen elements including U and Pb were analyzed for trace element concentrations by LA-ICP-MS. However, the concentrations of Li, Sc, Cr, and Sb are generally below or around the detection limits. Table 3 presents only the analytical results

Table 3. LA-ICP-MS Trace Element Concentrations (ppm) of Cassiterites from the Kuntabin Sn-W Deposit

| Spot	Al	Ti	Fe	Zr	Nb	Ta	W	U	Comment
KTB-cst-1	12.6	5,608	1,127	297	4,296	321	384	8.6	Cst-I
KTB-cst-2	8.8	4,733	899	303	3,071	1,587	144	5.6	Cst-I
KTB-cst-3	13.8	4,362	1,153	294	4,123	963	233	7.6	Cst-I
KTB-cst-4	7.9	3,511	962	185	3,398	1,070	245	5.6	Cst-I
KTB-cst-5	13.0	4,563	1,145	288	3,865	1,063	344	8.2	Cst-I
KTB-cst-6	8.6	5,053	880	329	3,424	329	366	8.0	Cst-I
KTB-cst-7	8.8	4,458	496	259	1,772	152	689	11.4	Cst-I
KTB-cst-8	18.0	3,845	253	143	107	64	7	0.7	Cst-II
KTB-cst-9	25.5	4,650	416	260	200	78	15	1.6	Cst-II
KTB-cst-10	26.7	4,880	408	239	254	159	15	2.0	Cst-II
KTB-cst-11	34.5	6,170	515	277	231	27	20	2.1	Cst-II
KTB-cst-12	3.0	1,132	145	44	196	524	2	0.1	Cst-II
KTB-cst-13	43.3	7,250	714	368	681	332	30	3.0	Cst-II
KTB-cst-14	36.7	7,389	814	338	757	462	28	3.0	Cst-II
KTB-cst-15	26.2	4,374	364	240	222	134	12	1.3	Cst-II
KTB-cst-16	6.2	2,407	154	129	118	273	4	0.5	Cst-II
KTB-cst-17	22.8	4,907	411	254	247	73	12	1.4	Cst-II
KTB-cst-18	11.6	3,754	589	182	1,037	1,129	28	1.1	Cst-II
KTB-cst-19	18.3	5,036	371	151	199	327	9	0.8	Cst-II
KTB-cst-20	25.8	5,405	456	257	328	119	13	1.6	Cst-II
KTB-cst-21	19.9	4,600	377	241	170	107	12	1.4	Cst-II
KTB-cst-22	18.4	3,676	355	215	318	265	14	1.4	Cst-II
KTB-cst-23	27.7	4,381	441	212	174	34	17	1.4	Cst-II
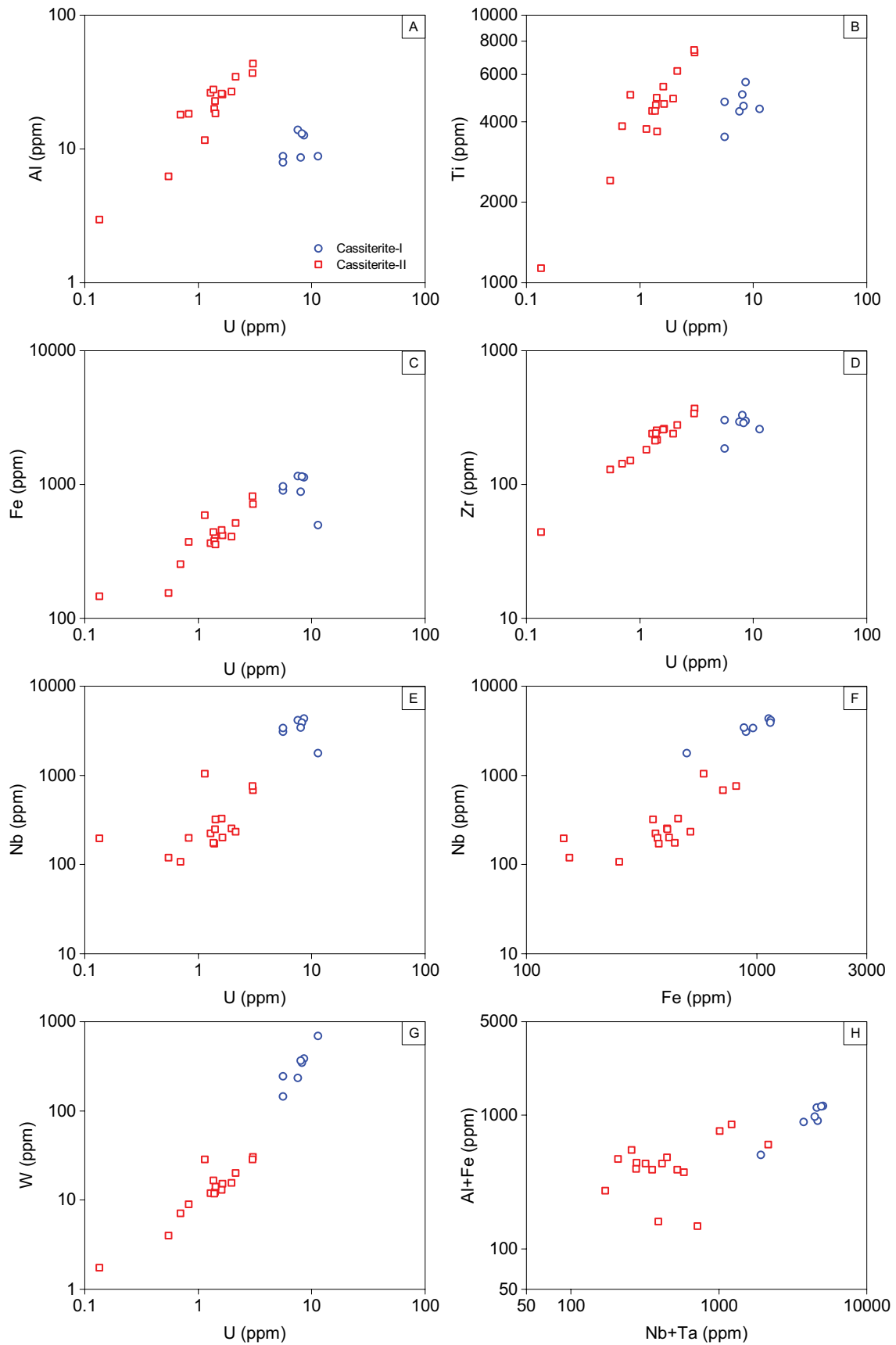
Fig. 7. (A-H) Trace element contents of cassiterite from the Kuntabin Sn-W deposit.

above the detection limits for Cst-I and Cst-II. These two generations of cassiterite show quite distinctive trace element patterns (Fig. 7). Trace element concentrations in Cst-I typically cluster in a small range, and a positive correlation is only observed between U and W (Fig. 7G). In contrast, in Cst-II the concentrations of Al, Ti, Fe, Zr, Nb, and W all display positive correlations with U. General positive correlations can be observed in element pairs of Fe-Nb and U-W for the whole data range from both Cst-I and Cst-II. Element groups of Nb + Ta and Al + Fe show only weak positive correlation.

The U concentrations of Cst-I range from 5.60 to 11.42 ppm, with an average of ~7.86 ppm. In contrast, U contents in Cst-II range from 0.14 to 3.05 ppm, with a much lower average of ~1.48 ppm. Cst-I consistently hosts more Fe (avg ~952 ppm), Nb (avg ~3,421 ppm), and W (avg ~344 ppm), compared to the same elements in Cst-II (avg ~424 ppm for Fe, ~327 ppm for Nb, and ~15 ppm for W). Variations of Al, Ti, and Zr in Cst-I are much smaller than in Cst-II (Fig. 7).

Cassiterite EMPA spot analysis and mapping

Spot analyses reveal that Sn is the only major element in cassiterite with average SnO_2 above 99.7 wt % (Table 4). The contents of MnO, Al_2O_3, WO_3, Ta_2O_5, In_2O_3, and UO_2 are generally below the detection limits. The order of magnitude contents of FeO, Nb_2O_5, and TiO_2 are the same as those revealed by the LA-ICP-MS analysis. Cst-I contains the highest FeO, with an average of ~0.17 wt %. Nb_2O_5 and TiO_2 contents in Cst-I are on average ~0.53 and ~0.26 wt %, respectively. FeO, Nb_2O_5, and TiO_2 contents in Cst-II are around the detection limits. The valid data (above the detection limit) are on average ~0.08 wt % for FeO, ~0.21 wt % for Nb_2O_5, and ~0.23 wt % for TiO_2. All the analyzed

trace elements are below the detection limits for Cst-III. Figure 8 clearly shows that the earlier generations of cassiterite consistently contain higher Fe, Nb, and Ti compared to later-stage cassiterites, while Al, Ta, U, and W are too low to be detected.

Cassiterite U-Pb age

Table 5 presents the analytical results of U and Pb isotopes and related parameters. Owing to the high content of common Pb in cassiterite, the Tera-Wasserburg U-Pb concordia diagram is used, and the age is obtained from the lower intercept in this plot. Spots from both Cst-I and Cst-II show very good linear correlations. Cst-I returned a lower intercept value of 87.9 ± 2.4 (2σ; MSWD = 0.20), and Cst-II returned a lower intercept value of 88.2 ± 4.0 (2σ; MSWD = 0.12). Therefore, ages of these two texturally distinct generations of cassiterite are indistinguishable with the current resolution of the analytical method. In combination, they yielded a lower intercept value of 88.1 ± 1.9 Ma (2σ; MSWD = 0.15; Fig. 9).

Molybdenite Re-Os age

Analytical results of Re-Os isotopes of molybdenite are listed in Table 6. Rhenium content is on average ~2.16 ppm and Os content is on average ~1.98 ppb in molybdenite. The molybdenite Re-Os model age is calculated as follows:

$$t = \frac{1}{\lambda} \ln\left(\frac{1+^{187}Os}{^{187}Re}\right) \quad (1)$$

The decay constant (λ) of ^{187}Re is 1.666×10^{-11} a^{-1} (Smoliar et al., 1996).

Five molybdenite samples from the Kuntabin deposit yielded consistent model ages, with a weighted mean age of 87.7 ±

Table 4. EMPA Analysis of Cassiterite from the Kuntabin Sn-W Deposit (wt %)

Sample	FeO	Nb_2O_5	TiO_2	SnO_2	Total	Comment
KTB-16-1	0.10	0.27	0.19	99.00	99.56	Cst-I
KTB-16-2	0.07	0.22	0.08	99.60	99.97	Cst-I
KTB-16-7	0.28	0.86	0.51	97.59	99.24	Cst-I
KTB-16-8	0.31	0.81	0.55	97.75	99.41	Cst-I
KTB-16-14	0.13	0.45	0.10	99.15	99.83	Cst-I
KTB-16-15	0.13	0.50	0.11	99.02	99.75	Cst-I
KTB-16-19	0.17	0.68	0.30	98.79	99.95	Cst-I
KTB-16-20	0.16	0.47	0.27	99.34	100.24	Cst-I
KTB-16-5	-	-	0.26	99.59	99.85	Cst-II
KTB-16-6	-	-	0.24	99.72	99.96	Cst-II
KTB-16-9	-	-	-	100.11	100.11	Cst-II
KTB-16-10	-	-	-	100.74	100.74	Cst-II
KTB-16-16	0.07	0.26	-	100.41	100.73	Cst-II
KTB-16-17	0.06	0.16	0.08	99.69	99.99	Cst-II
KTB-16-18	0.09	-	0.12	99.98	100.19	Cst-II
KTB-16-21	0.08	-	0.43	100.08	100.59	Cst-II
KTB-16-22	0.07	-	0.26	99.85	100.18	Cst-II
KTB-16-23	-	-	-	100.32	99.34	Cst-II
KTB-16-24	-	-	-	100.16	99.59	Cst-II
KTB-16-3	-	-	-	99.98	99.98	Cst-III
KTB-16-4	-	-	-	99.91	99.91	Cst-III
KTB-16-11	-	-	-	99.98	99.98	Cst-III
KTB-16-12	-	-	-	99.85	99.85	Cst-III
KTB-16-13	-	-	-	99.93	99.93	Cst-III
KTB-16-25	-	-	-	100.93	100.93	Cst-III
KTB-16-26	-	-	-	99.70	99.70	Cst-III
KTB-16-27	-	-	-	100.07	100.07	Cst-III
KTB-16-28	-	-	-	101.08	101.08	Cst-III

Note: Dashes indicate that analyzed elements are below detection limit
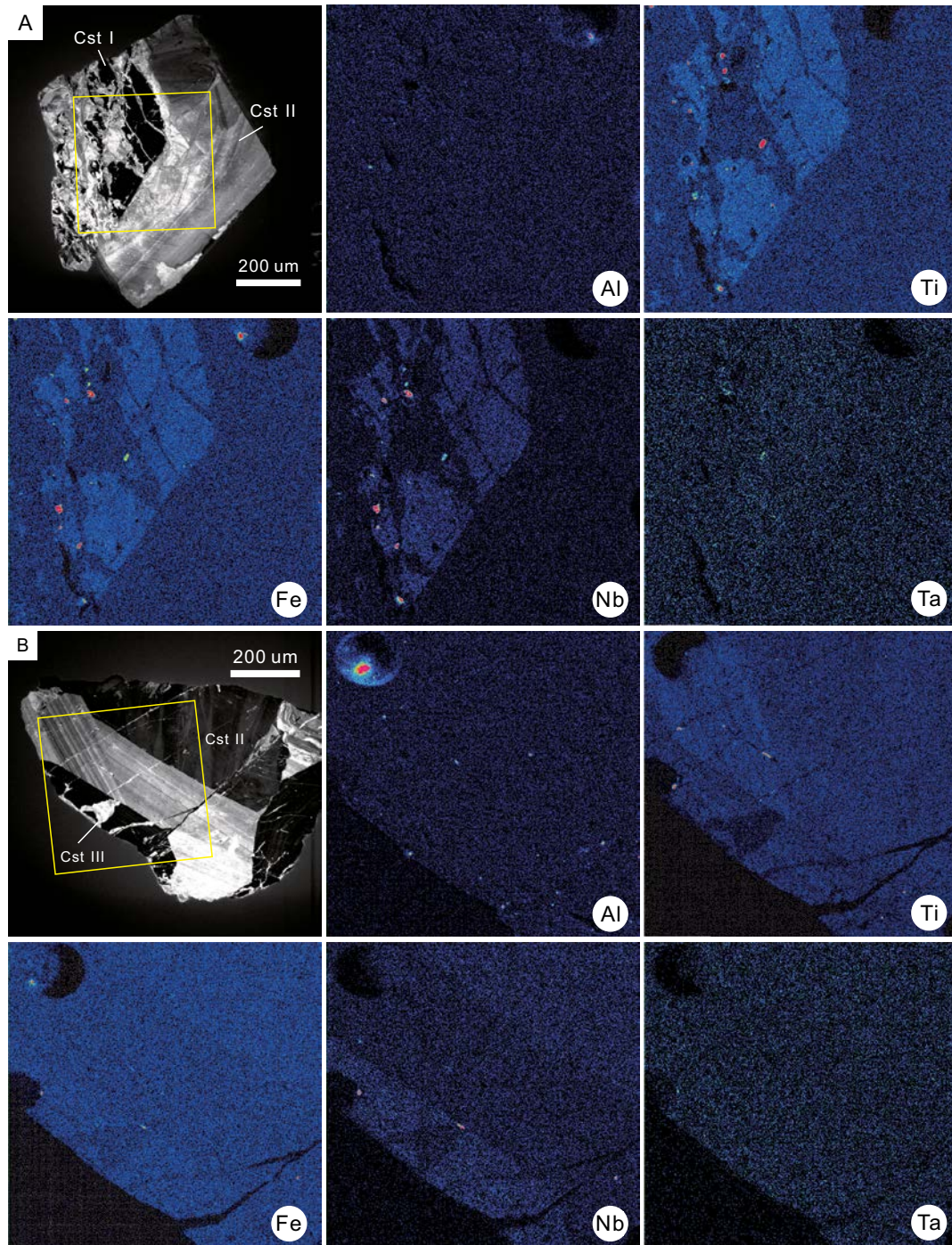
Fig. 8. (A, B) EMPA mapping of cassiterite. Brightness of figures for Al, Nb, and Ta have been slightly increased for better demonstration of microtextures.

0.5 Ma (2σ; MSWD = 1.5) and an isochron age of 88.7 ± 2.7 Ma (2σ; MSWD = 1.8; Fig. 10).

Discussion

Formation age of the Kuntabin Sn-W deposit

The lower intercept of the cassiterite U-Pb data in the Tera-Wasserburg concordia indicates that Sn and W mineralization

in the Kuntabin deposit occurred around 88.1 ± 1.9 Ma. Petrography of quartz-bearing veins from the Kuntabin deposit shows that molybdenite and cassiterite are closely related (Fig. 4) and crystallized from the hydrothermal fluid that formed the Kuntabin deposit. The identical Re-Os weighted mean model age (87.7 ± 0.5 Ma) and isochron age (88.7 ± 2.7 Ma) of the cogenetic molybdenite confirms the cassiterite mineralization age. These mineralization ages overlap with

Table 5. U-Pb Isotope Ratios of Cassiterites from the Kuntabin Sn-W Deposit

Spot	Th (ppm)	U (ppm)	Th/U	$^{207}Pb/^{206}Pb$		$^{207}Pb/^{235}U$		$^{206}Pb/^{238}U$		Comment
				Ratio	1σ	Ratio	1σ	Ratio	1σ	
KTB-16-1	0.00	3.19	0.00	0.1490	0.0283	0.2727	0.0483	0.0162	0.0008	Cst-I
KTB-16-4	0.02	6.45	0.00	0.1741	0.0252	0.3690	0.0476	0.0166	0.0008	Cst-I
KTB-16-6	0.00	14.38	0.00	0.1418	0.0089	0.2995	0.0185	0.0157	0.0003	Cst-I
KTB-16-7	0.00	12.09	0.00	0.1200	0.0118	0.2538	0.0233	0.0156	0.0004	Cst-I
KTB-16-8	0.01	5.46	0.00	0.4047	0.0225	1.6476	0.0908	0.0301	0.0008	Cst-I
KTB-16-12	0.10	4.43	0.02	0.4323	0.0343	1.9274	0.1266	0.0336	0.0011	Cst-I
KTB-16-13	0.01	6.08	0.00	0.3076	0.0236	0.9721	0.0735	0.0236	0.0008	Cst-I
KTB-16-23	0.00	12.75	0.00	0.0682	0.0103	0.1372	0.0202	0.0144	0.0005	Cst-I
KTB-16-24	0.00	10.63	0.00	0.0493	0.0078	0.0896	0.0138	0.0137	0.0005	Cst-I
KTB-16-28	0.00	15.83	0.00	0.0840	0.0119	0.1821	0.0262	0.0149	0.0004	Cst-I
KTB-16-29	0.00	12.61	0.00	0.1893	0.0131	0.4780	0.0340	0.0178	0.0004	Cst-I
KTB-16-30	0.00	17.36	0.00	0.0455	0.0067	0.0904	0.0153	0.0137	0.0005	Cst-I
KTB-16-32	0.00	6.96	0.00	0.1725	0.0136	0.3780	0.0274	0.0168	0.0005	Cst-I
KTB-16-2	0.02	1.26	0.01	0.6512	0.0668	3.3605	0.2592	0.0492	0.0026	Cst-II
KTB-16-3	0.02	2.95	0.01	0.4403	0.0288	1.7111	0.0995	0.0306	0.0014	Cst-II
KTB-16-9	0.02	0.27	0.06	1.7162	0.6953	8.0423	1.1950	0.0948	0.0131	Cst-II
KTB-16-11	0.15	3.47	0.04	0.5485	0.0367	4.9228	0.3309	0.0651	0.0022	Cst-II
KTB-16-14	0.08	0.67	0.11	0.6920	0.0841	3.9027	0.3516	0.0549	0.0032	Cst-II
KTB-16-15	0.04	0.35	0.12	0.4833	0.1614	1.2688	0.2382	0.0265	0.0029	Cst-II
KTB-16-16	0.06	2.36	0.02	0.4092	0.0460	1.8639	0.2096	0.0322	0.0015	Cst-II
KTB-16-17	0.01	4.48	0.00	0.0540	0.0142	0.0989	0.0276	0.0143	0.0010	Cst-II
KTB-16-18	0.01	1.46	0.01	0.4139	0.1746	0.6242	0.1132	0.0190	0.0019	Cst-II
KTB-16-19	0.01	11.29	0.00	0.0446	0.0074	0.0898	0.0143	0.0138	0.0005	Cst-II
KTB-16-20	0.02	9.59	0.00	0.1340	0.0184	0.3066	0.0411	0.0162	0.0007	Cst-II
KTB-16-21	0.00	2.01	0.00	0.3500	0.0485	0.9785	0.1181	0.0232	0.0013	Cst-II
KTB-16-22	0.00	1.88	0.00	0.2340	0.0464	0.6765	0.0852	0.0194	0.0011	Cst-II
KTB-16-25	0.03	2.61	0.01	0.1773	0.0238	0.3758	0.0448	0.0169	0.0007	Cst-II
KTB-16-26	0.01	2.30	0.01	0.1489	0.0484	0.2361	0.0575	0.0147	0.0012	Cst-II
KTB-16-27	0.01	1.71	0.01	0.1871	0.0295	0.4287	0.0767	0.0170	0.0016	Cst-II

the formation age of the two-mica granite (weighted mean $^{206}Pb/^{238}U$ age of 90.1 ± 0.7 Ma) and therefore indicate that the Sn-W mineralization is genetically related to the granite.

Cassiterite mineralization in the Kuntabin Sn-W deposit

Microtextures and trace elements of cassiterite: CL is a powerful tool in revealing the complicated microtextures of min-
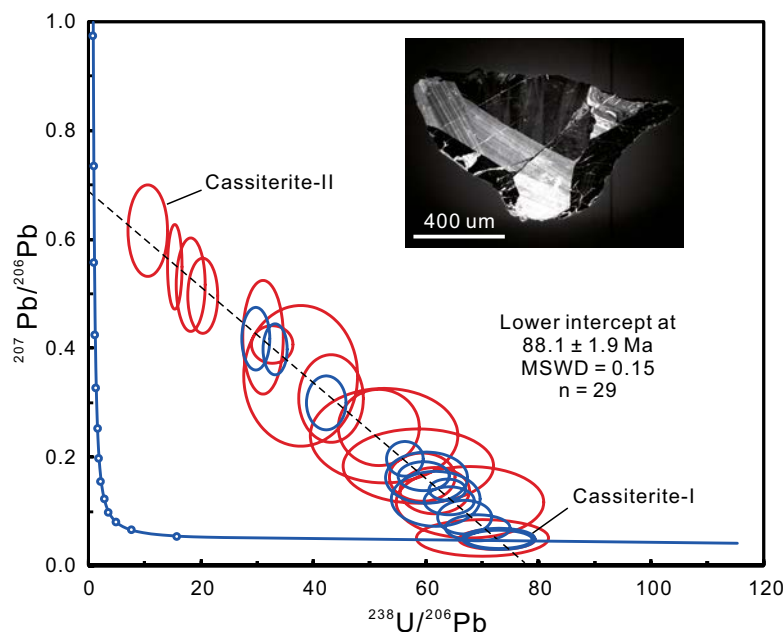

Fig. 9. Tera-Wasserburg U-Pb concordia diagram for cassiterite from the Kuntabin Sn-W deposit. Data points are in 2σ error. Inset is the CL image of a cassiterite crystal. MSWD = mean square of weighted deviates.

Table 6. Re-Os Isotopes of Molybdenite from the Kuntabin Sn-W Deposit

Sample	Weight (g)	Re (µg/g)		^{187}Re (µg/g)		^{187}Os (ng/g)		Model age (Ma)	
		Measured	2σ	Measured	2σ	Measured	2σ	Measured	2σ
JDC	0.0275	23.3127	0.0876	14,653	55.1	34.33	0.25	140.5	1.2
JDC	0.0265	23.9997	0.0944	15,085	59.3	35.14	0.23	139.7	1.1
KTB-mb-1	0.1569	2.2789	0.0063	1,432	4.0	2.12	0.03	88.6	1.2
KTB-mb-2	0.0094	2.9420	0.0086	1,842	5.4	2.69	0.02	87.7	1.8
KTB-mb-3	0.1452	1.9355	0.0091	1,217	5.7	1.77	0.02	87.3	1.2
KTB-mb-4	0.0476	2.0883	0.0116	1,313	7.3	1.89	0.04	86.2	1.7
KTB-mb-5	0.0887	2.3570	0.0102	1,482	6.4	2.17	0.01	87.7	0.6

erals that are otherwise not obvious (Smith and Stenstrom, 1965; Sippel, 1968; Rusk and Reed, 2002; Mao et al., 2017, 2018; Cheng et al., 2019). The Kuntabin Sn-W deposit has experienced at least three stages of cassiterite mineralization. Each stage displays distinctive CL textures and trace element patterns. Cst-I and Cst-II both formed large euhedral crystals with thin oscillatory zones. CL intensity of Cst-II is much higher than Cst-I, but in contrast, Cst-I contains more Fe, Nb, and Ti (Fig. 7). Figure 8 shows that Cst-II contains more Fe, Nb, and Ti compared to Cst-III. As revealed by previous studies, Al, Ti, and W are the luminescence activators, but Fe quenches the luminescence of cassiterite (Remond, 1973; Farmer et al., 1991). Average contents of Al (~10.5 ppm) and Ti (~4,613 ppm) in Cst-I are slightly lower than or comparable to those in Cst-II (~22.8 ppm Al; ~4,616 ppm Ti). Average content of W (~344 ppm) in Cst-I is over 20 times that in Cst-II (~15 ppm). These activator elements should be able to generate more intense luminescence in Cst-I, which, in contrast, shows black CL intensity. Therefore, although the Fe contents in Cst-II are only double those in Cst-I, the quenching effect of Fe (and Nb) overwhelms the activating effect of Al, Ti, and W, leading to the very low CL intensity. Iron content in Cst-III could not be analyzed by LA-ICP-MS owing to small size and irregular shape of Cst-III, but the EMPA spot analysis and mapping clearly demonstrate that Cst-III contains less Fe (below detection limit of EMPA), consistent with its extremely high CL intensity under the same analytical conditions.

Based on the ionic radius, charge balance, and coordination of ions with respect to Sn^{4+}, trace elements incorporated in cassiterite are inferred to be in the following valence states: Al^{3+}, Fe^{3+}, Sc^{3+}, Cr^{3+}, Sb^{3+}, Ti^{4+}, Zr^{4+}, W^{4+}, U^{4+}, Nb^{5+}, and Ta^{5+} (Möller et al., 1988; Plimer et al., 1991; Murciego et al., 1997; Tindle and Breaks, 1998; Cheng et al., 2019). Quadrivalent elements can directly substitute Sn^{4+}, without the requirement of charge balance. In contrast, compensation of other elements is necessary for the incorporation of the trivalent and pentavalent elements, e.g., $Fe^{3+} + Ta^{5+} = Sn^{4+}$ and $Al^{3+} + H^+ = Sn^{4+}$. However, the sum of the analyzed trivalent elements is notably less than the sum of the analyzed pentavalent elements (Fig. 7H). The analyzed Li, Sc, Cr, and Sb contents are generally below the detection limits and, therefore, cannot be the compensation elements. We speculate that H^+, which is not capable of being analyzed by LA-ICP-MS or EMPA, may be a significant charge balance element, as previously proposed (Möller et al., 1988; Plimer et al., 1991; Murciego et al., 1997; Tindle and Breaks, 1998; Cheng et al., 2019).

Oscillatory zoning of cassiterite: Compositional zoning of cassiterite may be generated by (1) progressive changes of bulk fluid composition during magmatic-hydrothermal evo-
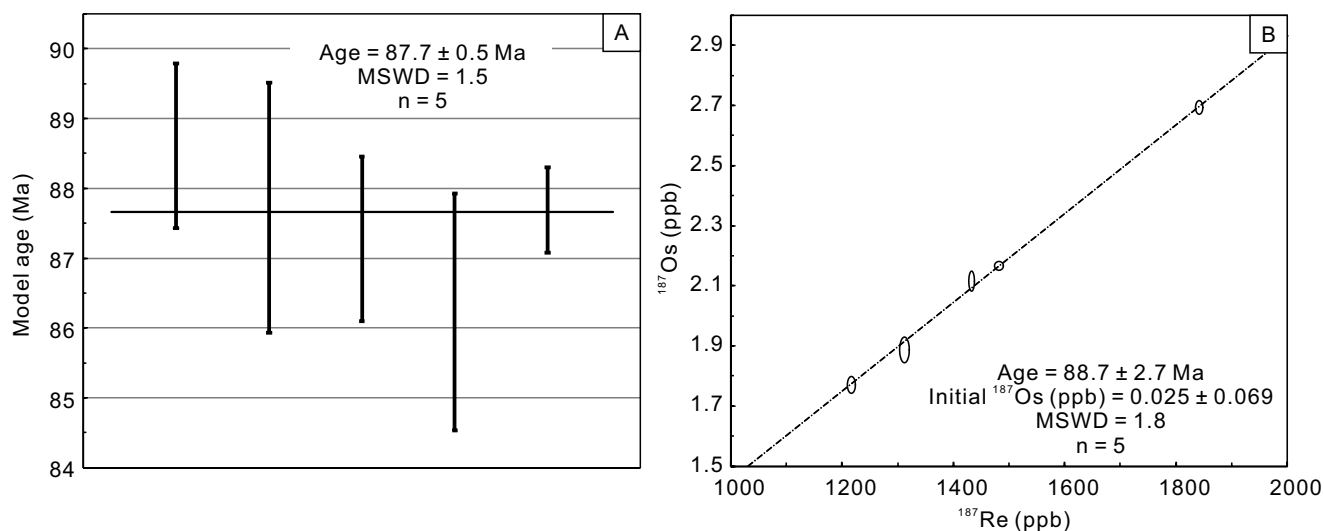

Fig. 10. Weighted mean model age (A) and isochron age (B) of molybdenite from the Kuntabin Sn-W deposit. MSWD = mean square of weighted deviates.

lution, (2) local fluctuations of hydrothermal fluid composition near the growing crystal surface, and (3) variations of available lattice sites on different crystal faces during crystal growth in hydrothermal fluid (Farmer et al., 1991). Cst-I is relatively homogeneous in both CL textures and trace element concentrations, indicating that Cst-I crystallized under relatively stable physical-chemical conditions. In contrast, oscillatory zones of Cst-II are clearer compared to Cst-I and Cst-III. Compositional variations in Cst-II are very significant and may approach two orders of magnitude. The bulk composition of the ore-forming fluid is not likely to change so dramatically in a single stage of fluid evolution. Positive correlations among nearly all the analyzed elements clearly indicate that these elements were incorporated kinetically under high crystallization rate rather than by equilibrium incorporation during cassiterite growth (Rusk, 2012; Mao et al., 2017). Therefore, the fine oscillatory zones in Cst-II are the product of local compositional fluctuation of the hydrothermal fluid during rapid cassiterite crystallization. Crystal-scale variations of CL intensity have also been recorded in Cst-II (Figs. 5C, 8). FeO content is relatively homogeneous, but the content of Nb shows negative correlation with CL intensity, indicating that the Nb in cassiterite may also serve as a CL block like Fe and that trace elements are preferentially incorporated into different crystal faces.

Evolution of the magmatic-hydrothermal system: The distinctive CL textures and composition patterns of three stages of cassiterite clearly indicate that they were formed under different physical-chemical conditions. Breccia-related Sn-W deposits are scarcely reported in the Southeast Asian tin belt (e.g., Clegg, 1944a; Yeap, 1978; Leong, 1985; Wang et al., 2014) and only account for ~1% of the of all the primary Sn-W deposits in Southeast Asia, largely due to the relatively deep emplacement of the ore-forming granites (Schwartz et al., 1995). Although no breccia was observed in the Kuntabin deposit during our field work, grain-scale brecciation is well documented in cassiterite grains. Based on the brecciation of Cst-I and the fracture of Cst-I and Cst-II, we infer that frequent seismic events occurred to generate channels and spaces for the input of ore-forming fluid. Breccia and fracture of the sealed hydrothermal veins not only lead to sudden pressure release but also will cause significant temperature drop through adiabatic cooling (Fournier, 1999; Heinrich et al., 2005; Henley et al., 2015; Mercer et al., 2015; Mao et al., 2017), which may have facilitated the precipitation of Sn and W. The erosion of Cst-I into rounded cores indicates the input of more acidic hydrothermal fluid that can dissolve and reprecipitate cassiterite and other minerals (Rusk, 2012). More Al

will be dissolved into the hydrothermal fluid by the interaction between more acidic fluid and the hosting granite. We infer that the doubled average Al content in Cst-II compared to that of Cst-I is partly related to the higher concentration of Al available in the hydrothermal fluid. Nearly all the other analyzed elements are higher in Cst-I than Cst-II, except for Al and Ti (Fig. 7). The substitution of Fe in cassiterite is directly related to Fe concentration in the bulk fluid (Farmer et al., 1991); therefore, the distinctive contents of Fe (as well as Zr, Nb, Ta, W, and Pb) in different stages of cassiterite, in combination with the characteristic CL textures, clearly demonstrate the episodic input of compositionally different ore-forming fluids during the magmatic-hydrothermal evolution of the Kuntabin Sn-W deposit. The Ti/Zr ratios of cassiterite from the Gejiu tin district in China vary over an order of magnitude, reflecting the progressive depletion of Ti relative to Zr in the hydrothermal fluid as it migrated and evolved away from the intrusion (Cheng et al., 2019). In contrast, the two distinctive generations of cassiterite in the Kuntabin deposit exhibit relatively stable Ti/Zr ratios, ranging between 15 to 19 for Cst-I and 17 to 33 for Cst-II. Rutile needles are observed in quartz-bearing veins formed during the cassiterite mineralization, but hydrothermal zircon is not present. Therefore, these elements entered cassiterite in a Ti-saturated but Zr-unsaturated system. The slight difference of Ti/Zr ratios in Cst-I and Cst-II may be easily achieved by local fluctuations during cassiterite crystallization, although compositional variation in hydrothermal fluid cannot be excluded.

Magma sources of the ore-related granites

Zircon $\varepsilon_{Hf}(t)$ values of the Kuntabin Sn-W deposit range from –16.0 to –8.9, with an average of ~–12.6 (Table 7). Zircon $\varepsilon_{Hf}(t)$ values of the Hermyingyi Sn-W deposit vary from –14.5 to –10.7, with an average of ~–12.8 (Table 7; Jiang et al., 2017; W. Mao et al., unpub. data, 2019). The Dapingba Mo-W deposit in northern Myanmar has much higher zircon $\varepsilon_{Hf}(t)$ values from –9.3 to 2.4, with an average of ~–1.8 (Li, J.X., et al., 2018). The Shangalon porphyry Cu-Au deposit in the West Burma terrane has the highest zircon $\varepsilon_{Hf}(t)$ from 0.0 to 2.9, with an average of ~1.5 (Gardiner et al., 2018; Li, J.X., et al., 2018). The calculated two-stage model ages are on average 1950 Ma for the Kuntabin Sn-W deposit and 1940 Ma for the Hermyingyi Sn-W deposit. In contrast, the Dapingba Mo-W deposit and Shangalon Cu-Au deposit have much younger T_{DM2} on average, around 1285 and 1018 Ma, respectively (Gardiner et al., 2018; Li, J.X., et al., 2018). The ore-forming diorite porphyry in the Shangalon Cu-Au deposit has mantle-like zircon oxygen isotope values ($\delta^{18}O = 5.5 \pm$

Table 7. Compiled Re Contents in Molybdenites and $\varepsilon_{Hf}(t)$ Values of Zircons from Deposits in Myanmar

Deposit	Re (ppm)			$\varepsilon_{Hf}(t)$			T_{DM2} (Ma)			References
	Minimum	Maximum	Average	Minimum	Maximum	Average	Minimum	Maximum	Average	
Shangalon	70.37	70.37	70.37	0.0	2.9	1.5	930	1110	1018	J.X. Li et al. (2018), Gardiner et al. (2018)
Dapingba	2.45	19.25	7.39	–9.3	2.4	–1.8	1015	1760	1285	J.X. Li et al. (2018)
Kuntabin	1.94	2.94	2.32	–16.0	–8.9	–12.6	1712	2161	1950	This study
Mawchi	1.36	1.36	1.36							Myint et al. (2018)
Hermyingyi	0.002	0.027	0.014	–14.5	–10.7	–12.8	1806	2042	1940	W. Mao et al. (unpub. data, 2019)

0.4‰) and was inferred to originate from partial melting of metasomatized mantle (Gardiner et al., 2016a, b, 2018; Li, J.X., et al., 2018). Ore-forming granite in the Dapingba Mo-W deposit has intermediate zircon $\varepsilon_{Hf}(t)$ values and was derived from partial melting of ancient continental crust with minor addition of mantle material (Li, J.X., et al., 2018). In contrast, the Sn-W–related granites are the products of partial melting of the Paleoproterozoic continental crust and contain minimal mantle contribution.

Rhenium contents in molybdenites from the Kuntabin deposit lie in a narrow range from 1.94 to 2.36 ppm, with an average of ~2.16 ppm (Fig. 11; Table 7). Molybdenites from the Hermyingyi Sn-W deposit have much lower Re contents, ranging from 8.9 to 27 ppb. The only molybdenite sample analyzed from the Mawchi deposit, the largest Sn-W deposit in Myanmar, contains 1.36 ppm Re (Myint et al., 2018). Molybdenites from the Dapingba Mo-W deposit contain on average ~7.39 ppm Re, with the highest content of 19.25 ppm (Li, J.X., et al., 2018). In contrast, molybdenite from the Shangalon Cu-Au deposit contains 70.37 ppm Re (Fig. 1; Li, J.X., et al., 2018), which is much higher than Sn-W deposits in the Sibumasu and Tengchong terranes. Re contents in molybdenites generally show a positive correlation with the zircon $\varepsilon_{Hf}(t)$ values of the ore-forming granites (Fig. 11B).

The amount of Re in molybdenite has long been related to various types of deposits (Zhirov and Ivanoca, 1959). Giles

and Schilling (1972) showed that molybdenite from porphyry Cu deposits contains higher Re (mean = 660 ppm) than that from porphyry Mo and quartz-vein deposits (mean = 47 ppm). Recent studies and compilations of data all confirmed that molybdenites from porphyry Cu (Mo) deposits contain the highest Re, mainly distributed in the range of >100 to over 10,000 ppm, Re of molybdenites from porphyry Mo (Cu) deposits mainly lies between 10 and 100 ppm, and molybdenites from greisen Sn-W deposits typically have <10 ppm down to subparts-per-million levels of Re content (Mao et al., 1999; Berzina et al., 2005; Sinclair et al., 2009; Pašava et al., 2016). Rhenium is moderately incompatible during mantle melting (Shirey and Walker, 1998). Metal source of the deposit and degree of magma fractionation have been inferred to be the key factors that control the Re contents of molybdenites in granite-related deposits, and the contents generally decrease with decreasing mantle contribution (Mao et al., 1999; Stein et al., 2001; Blevin, 2009; Sinclair et al., 2009). Our results for Re contents in molybdenites from Myanmar generally agree with those of previous studies. The broadly positive correlation with zircon $\varepsilon_{Hf}(t)$ values in the ore-forming granites suggests that the Re contents of molybdenites are predominantly controlled by the degree of mantle contribution in the investigated samples. Conversely, the coupled zircon $\varepsilon_{Hf}(t)$ values and Re concentrations in molybdenites can be used as an indicator of mantle contribution and a potential discriminator of ore deposit types. The Hermyingyi deposit hosts similar zircon Hf isotope signatures but much lower Re contents in molybdenites compared to the Kuntabin deposit (Fig. 11). Such variation indicates that other factors like temperature and oxygen fugacity may have influenced the incorporation of Re in molybdenite during the hydrothermal processes (Stein et al., 2001; Berzina et al., 2005; Voudouris et al., 2009).

Magmatism and Sn-W mineralization in the Western tin belt

Magmatic activities related to the Paleo-Tethys subduction (Eastern province) are very rarely reported in Myanmar and only distributed in the easternmost part of Myanmar, close to the border with Laos (Mitchell, 1981, 1986, 2018; Mitchell and Garson, 1981; Zaw, 1990; Mitchell et al., 2012; Gardiner et al., 2014, 2016a, b, 2018; Myanmar Geosciences Society, 2014). The Main Range S-type granites in Myanmar are limitedly distributed in the eastern part of the Shan Plateau and extend to west Yunnan in the north and west Thailand in the south (Fig. 1B; Wang et al., 2014, 2016; Gardiner et al., 2016a, b, 2018; Fanka et al., 2018; Mitchell, 2018). The Western province is widely distributed in Myanmar, west Yunnan, and west Thailand, which is equivalent to the western part of the Sibumasu terrane (Fig. 1; Mitchell, 1981, 1986, 2018; Mitchell et al., 2012; Wang et al., 2014; Gardiner et al., 2016a, b, 2018; Li, J.X., et al., 2018). Episodic magmatic activities occurred in the western Sibumasu terrane since the Jurassic owing to the successive accretion of the Gondwana-derived continental blocks (Barley et al., 2003; Searle et al., 2007; Mitchell et al., 2012; Gardiner et al., 2015, 2016a, b, 2018; Li, J.X., et al., 2018).

The Early to Mid-Jurassic magmatic activities (~185–165 Ma) are mainly distributed in the north part of the western Sibumasu terrane and have been attributed to the eastward (current direction, here and after) subduction of the
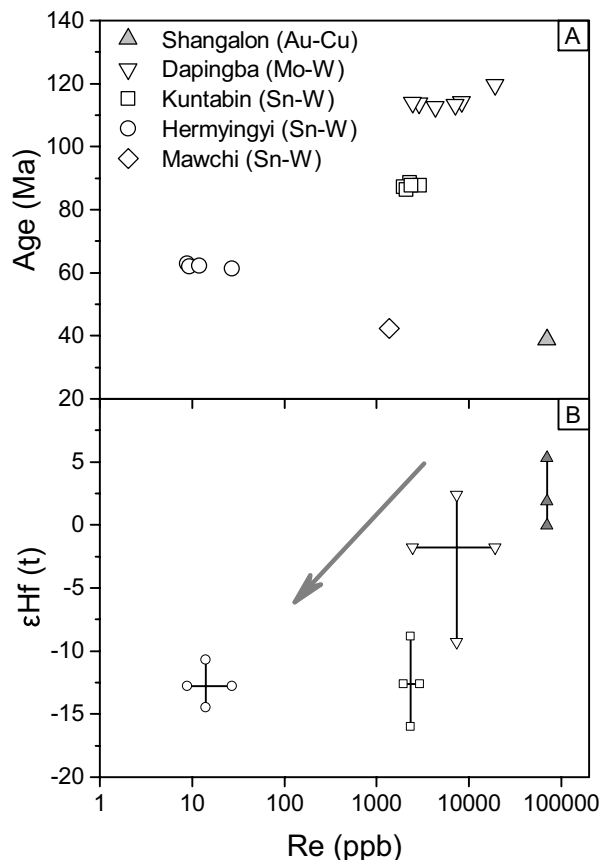

Fig. 11. (A) Re contents versus ages of molybdenite from deposits in Myanmar. (B) Re content in molybdenite versus $\varepsilon_{Hf}(t)$ of zircon from deposits in Myanmar.
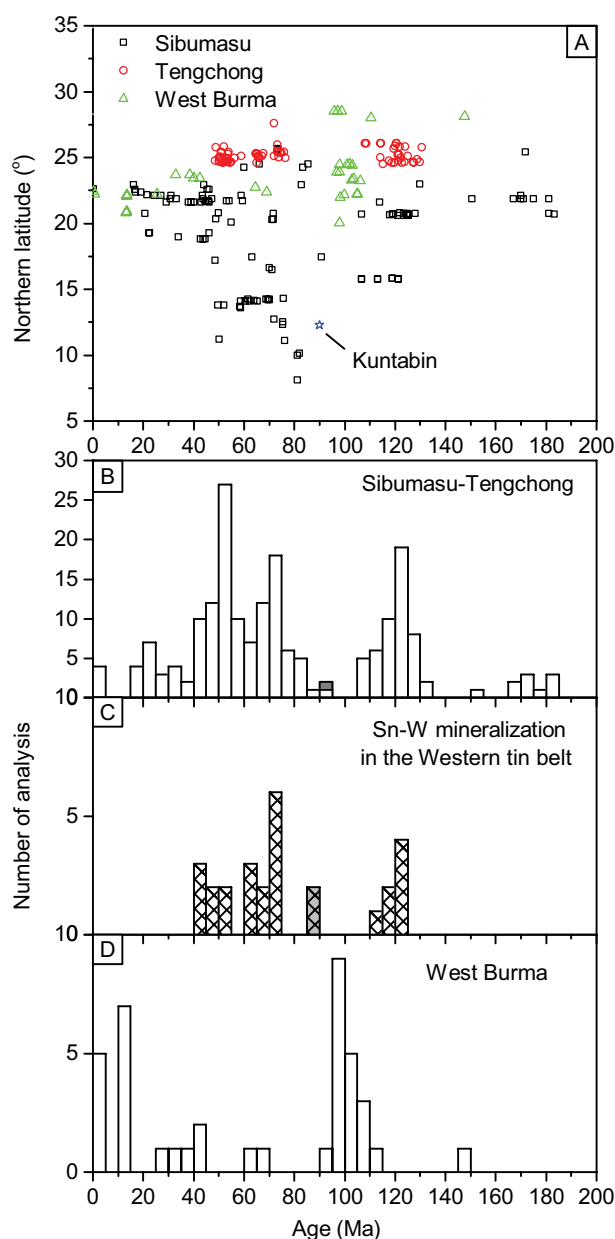
Fig. 12. (A) Summary of igneous rock zircon U-Pb ages from the Western tin belt (Sibumasu, Tengchong) and West Burma terrane and their northern latitude distribution. (B) Igneous rock zircon U-Pb ages from the Sibumasu and Tengchong terranes. (C) Sn-W mineralization ages of hydrothermal muscovite, molybdenite, and cassiterite from the Western tin belt. (D) Igneous rock zircon U-Pb ages from the West Burma terrane. Data from Barley et al. (2003), Searle et al. (2007), Mitchell et al. (2012), Dong et al. (2013), Yu et al. (2014), Gardiner et al. (2014, 2015a, 2016a, b, 2017, 2018), Xie et al. (2016), Cao et al. (2017), Crow and Zaw (2017), Jiang et al. (2017), H. Li et al. (2018), Dew et al. (2018), J.X. Li (2018), Lin et al. (2019), and references therein. The gray boxes are age data acquired from the Kuntabin deposit.

oceanic slab between the Tengchong and Sibumasu terranes (Figs. 12A-C, 13; Gardiner et al., 2018). The Early Cretaceous magmatic activities (~130–105 Ma) and related Sn-W mineralization are mainly reported in the Tengchong terrane and north part of the western Sibumasu terrane and are inferred

to form in a continental arc setting by the eastward subduction of the Meso-Tethys Ocean (e.g., Tieyaoshan Sn deposit: 119.3 ± 1.7 Ma, Chen et al., 2014; Dapingba Mo-W deposit: 113.7 ± 0.7 Ma, Li, J.X., et al., 2018; Figs. 1, 13). Magmatic cessation from ~105 to 90 Ma has been identified in the Tengchong and Sibumasu terranes, likely related to the collision between the West Burma terrane and the Tengchong-Sibumasu terranes along the Myitkyina suture zone, which represents the closure of the Meso-Tethys Ocean (Figs. 1, 12, 13; Barley et al., 2003; Searle et al., 2007; Mitchell et al., 2012; Metcalfe, 2013; Gardiner et al., 2015, 2016a, b, 2018; Liu et al., 2016a, b; Zhou et al., 2017; Li, J.X., et al., 2018; Mitchell, 2018; Lin et al., 2019). In contrast, the West Burma terrane developed abundant igneous rocks from ~115 to 90 Ma during the eastward subduction of the Neo-Tethys Ocean (Figs. 12, 13; Mitchell, 1993; Mitchell et al., 2012; Wang et al., 2014; Gardiner et al., 2016a, b; Li, J.X., et al., 2018; Lin et al., 2019).

Significant granite-related Sn-W mineralization occurred in Myanmar since the Late Cretaceous after the continuous subduction of the Neo-Tethys oceanic slab reached beneath the Tengchong-Sibumasu terranes (Mitchell, 1992, 2018; Charusiri et al., 1993; Mitchell et al., 2012; Sanematsu et al., 2014; Gardiner et al., 2016a, b, 2018; Jiang et al., 2017; Thein, 2017; Li, H., et al., 2018; Li, J.X., et al., 2018). The ancient lower crust was underplated by metasomatized mantle wedge-derived basaltic melts to form felsic magma required for successive Sn-W mineralization after melting, assimilation, storage, and homogenization (MASH) processes (Charusiri et al., 1993; Gardiner et al., 2016a, b, 2018; Li, J.X., et al., 2018). The granitic magma experienced high degrees of fractional crystallization and fluid exsolution to form a series of Sn-W deposits in the Western tin belt (Lehmann and Mahawat, 1989; Heinrich, 1990; Lehmann, 1990; Charusiri et al., 1993; Linnen and Williams-Jones, 1995; Schwartz et al., 1995; Li, J.X., et al., 2018). Compilation of previous radiogenic ages of hydrothermal muscovite, molybdenite, and cassiterite in the Tengchong and Sibumasu terranes shows that the Late Cretaceous Sn-W mineralization did not start until ~72 Ma (Fig. 12; Chhibber, 1934; Mitchell, 1986; Charusiri et al., 1993; Chen et al., 2014, 2015; Li, J.X., et al., 2018). Therefore, the cassiterite U-Pb age (~88.1 Ma) and molybdenite Re-Os isochron age (~88.7 Ma) for the Kuntabin deposit record the earliest Sn-W mineralization in the Tengchong-Sibumasu terranes that is related to the subduction of the Neo-Tethys Ocean.

The earliest Late Cretaceous magmatic activity in the Western tin belt reported so far is a diorite dike from the Mokpalin, which is ~110 km northeast of Yangon, with a zircon U-Pb age of 90.8 Ma (Fig. 12; Mitchell et al., 2012). The low I_{Sr} signature for the Mokpalin diorite dike implies a juvenile mantle origin (Mitchell et al., 2012). The compiled data show that the number of zircon U-Pb ages from the igneous rocks in the Tengchong-Sibumasu terranes increases gradually after 90 Ma (Fig. 12). Whole-rock and mineral Rb-Sr isochron dating of tin-related granites revealed ages of 84 and 92.9 ± 26.7 Ma in west Yunnan (Chen, 1987; Zhou et al., 2017), 94 ± 14 Ma in Parker Throtter of Myanmar (Cobbing et al., 1992), 93 ± 4 Ma in Khao Daen of mid Thailand, and 82 ± 4, 83 ± 7, 94 ± 12, and 98 ± 7 Ma in southwest Thailand (Putthapiban and Gray, 1983; Pollard et al., 1995). However, the Rb-Sr sys-
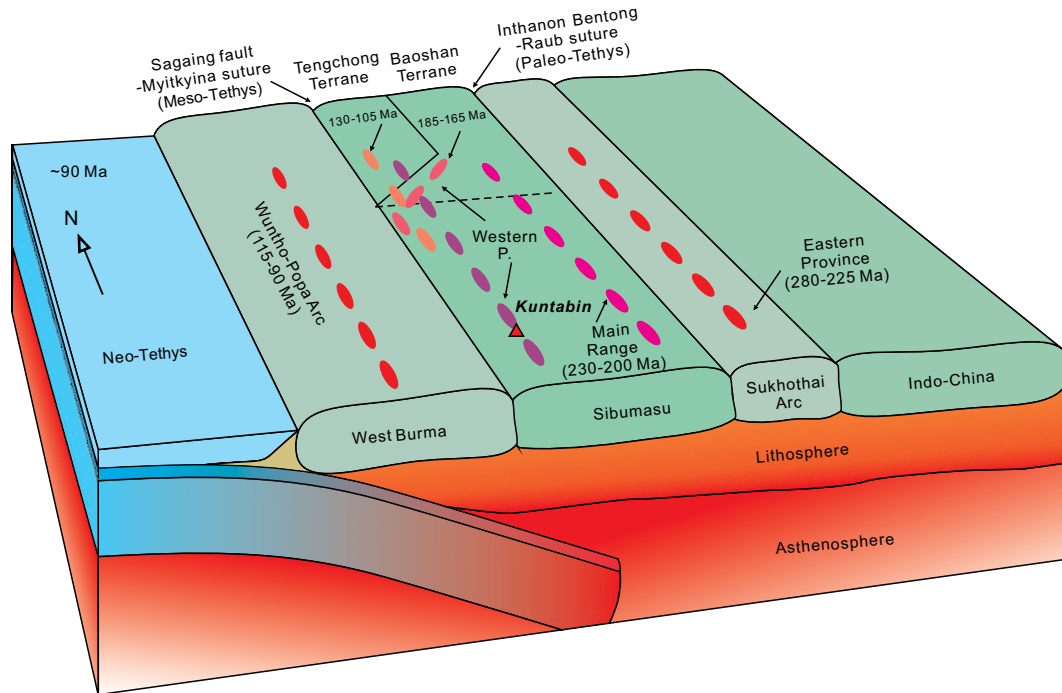
Fig. 13. Schematic tectonic model for the Southeast Asian granite provinces at ~90 Ma. Not to scale. Modified after Hutchison (1975), Mitchell (1977, 1986), Sengor (1979, 1984, 1987), MetCalfe (1984, 1988, 1998, 2011, 2013), Schwartz (1995), Searle et al. (2012), Gardiner et al. (2015a, 2016a, b, 2018), Mitchell et al. (2015), Ng et al. (2015a, b), J.X. Li et al. (2018), Wang et al. (2018), and references therein. Complicated structures in suture zones and within each terrane are simplified for better presentation of the general geologic setting. Color spheres refer to projections of granites on surface.

tem has a relatively low closure temperature and may easily be overprinted and reset by later geologic activities (Romer et al., 2007). We retain doubts about the accuracy of these Rb-Sr ages, especially those with very large errors. Nevertheless, we infer that, in combination with the zircon U-Pb ages in Kuntabin and Mokpalin, these ages indicate that, after the magmatic cessation related to the closure of the Meso-Tethys Ocean, magmatism and Sn-W mineralization initiated at ~90 Ma when the subducted slab of the Neo-Tethys Ocean reached beneath the Tengchong-Sibumasu terranes (Fig. 13). We infer that the lack of mineralization ages between ~89 and 72 Ma is due to the shortage of geochronological studies, and more deposits could be potentially explored in these areas. The West Burma terrane is currently not adjacent to west of southern Myanmar, because the opening of the Andaman Sea separated it from the West Sumatra block in the Miocene, and because right-lateral strike slip on the Sagaing fault moved it to the north (Mitchell, 1977, 1979, 1981, 1992; Mitchell and Garson, 1981; MetCalfe, 1996, 2011, 2013; Barber and Crow, 2009; Mitchell et al., 2012; Thein, 2017).

Conclusions

1. Combined zircon and cassiterite LA-ICP-MS U-Pb dating and molybdenite Re-Os dating reveal that Sn-W mineralization in the Kuntabin deposit occurred at ~88.1 ± 1.9 Ma, which is genetically related to the coeval two-mica granite with an intrusion age of ~90.1 ± 0.7 Ma. These ages record the earliest magmatism and Sn-W mineralization related to the eastward (current direction) subduction of

the Neo-Tethys oceanic slab beneath the Tengchong-Sibumasu terranes.

2. Three generations of cassiterite with distinctive CL textures and trace element patterns have been identified, but at least the first two generations are indistinguishable in ages with the resolution of the current analytical method. The distinctions in microtextures and trace element contents in cassiterite indicate the episodic input of ore-forming fluids and distinctive changes in the physical-chemical nature of the ore-forming system. Sudden changes of fluid pressure, temperature, and pH may have facilitated the deposition of Sn and W.

3. The quenching effects of Fe and Nb overwhelm the activating effects of Al, Ti, and W and dominate the CL textures in cassiterite.

4. The low concentrations of Re in molybdenite and negative zircon $\varepsilon_{Hf}(t)$ values from the greisen-type Sn-W deposits in Myanmar indicate that the ore-forming granites for these deposits were predominantly derived from melting of the Paleoproterozoic continental crust and contain minimal mantle contribution.

cant improvement of the original manuscript. We appreciate the assistance of Ja Mu during the field work in Myanmar. We also thank Drs. Youwei Chen, Xiang Li, Zhihui Dai, Shengling Sun, and Yezhi He and the people who helped us during the lab work.

REFERENCES

Barber, A.J., and Crow, M.J., 2009, Structure of Sumatra and its implications for the tectonic assembly of Southeast Asia and the destruction of Paleotethys: Island Arc, v. 18, p. 3–20.

Barley, M.E., Pickard, A.L., Zaw, K., Rak, P., and Doyle, M.G., 2003, Jurassic to Miocene magmatism and metamorphism in the Mogok metamorphic belt and the India-Eurasia collision in Myanmar: Tectonics, v. 22, doi: 10.1029/2002TC001398.

Beckinsale, R.D., 1979, Granite magmatism in the tin belt of Southeast Asia, *in* Atherton, M.P., and Tarney, J., eds., Origin of granite batholiths: Kent, Shiva Publishing, p. 34–44.

Bender, F., 1983, Geology of Burma: Stuttgart, Gebrüder Borntraeger, p. 1–295.

Berzina, A., Sotnikov, V.I., Economou-Eliopoulos, M., and Eliopoulos, D.G., 2005, Distribution of rhenium in molybdenite from porphyry Cu-Mo and Mo-Cu deposits of Russia (Siberia) and Mongolia: Ore Geology Reviews, v. 26, p. 91–113.

Blevin, P.L., 2009, The primacy of magma compositions in determining the Re and W contents of molybdenite: International Applied Geochemistry Symposium, 24th, Fredericton, Canada, 2009, Proceedings, p. 119–122.

Brown, J.C., and Heron, A.M., 1923, The geology and ore deposits of the Tavoy district: Memoirs of the Geological Survey of India, v. 44, p. 167–354.

Campbell, J.M., 1920, Tungsten deposits of Burma and their origin: Economic Geology, v. 15, p. 511–534.

Cao, H.W., Pei, Q.M., Zhang, S.T., Zhang, L.K., Tang, L., Lin, J.Z., and Zheng, L., 2017, Geology, geochemistry and genesis of the Eocene Lailishan Sn deposit in the Sanjiang region, SW China: Journal of Asian Earth Sciences, v. 137, p. 220–240.

Charusiri, P., Clark, A.H., Farrar, E., Archibald, D., and Charusiri, B., 1993, Granite belts in Thailand: Evidence from the ⁴⁰Ar/³⁹Ar geochronological and geological syntheses: Journal of Southeast Asian Earth Sciences, v. 8, p. 127–136.

Chen, J.S., 1987, Discussion on the age division and the selects of isotopic age determination for granitic rock in Western Yunnan: Yunnan Geology, v. 6, no. 2, p. 101–113 (in Chinese with English abs.).

Chen, X.C., Hu, R.Z., Bi, X.W., Li, H.M., Lan, J.B., Zhao, C.H., and Zhu, J.J., 2014, Cassiterite LA-MC-ICP-MS U/Pb and muscovite ⁴⁰Ar/³⁹Ar dating of tin deposits in the Tengchong-Lianghe tin district, NW Yunnan, China: Mineralium Deposita, v. 49, p. 843–860.

Chen, X.C., Hu, R.Z., Bi, X.W., Zhong, H., Lan, J.B., Zhao, C.H., and Zhu, J.J., 2015, Petrogenesis of metaluminous A-type granitoids in the Tengchong-Lianghe tin belt of southwestern China: Evidences from zircon U-Pb ages and Hf-O isotopes, and whole-rock Sr-Nd isotopes: Lithos, v. 212–215, p. 93–110.

Cheng, Y.B., Spandler, C., Kemp, A., Mao, J.W., Rusk, B., Hu, Y., and Blake, K., 2019, Controls on cassiterite (SnO₂) crystallization: Evidence from cathodoluminescence, trace-element chemistry, and geochronology at the Gejiu tin district: American Mineralogist, v. 104, p. 118–129.

Chhibber, H.L., 1934, The mineral resources of Burma: London, Macmillan, p. 1–320.

Clegg, E.L.G., 1944a, Bulletin no. 15. Notes on tin and wolfram with a description of the tin and wolfram deposits of India and Burma: Records of the Geological Survey of India, v. 76, p. 1–129.

——1944b, The mineral deposit of Burma: Bombay, Times of India Press, p. 1–64.

Cobbing, E.J., Mallick, D.I.J., Pitfield, P.E.J., and Teoh, L.H., 1986, The granites of the Southeast Asian tin belt: Journal of the Geological Society, London, v. 143, p. 537–550.

Cobbing, E.J., Pitfield, P.E.J., Derbyhire, D.P.F., and Mallick, D.I.J., 1992, The granites of the South-east Asian tin belt: British Geological Survey, Overseas Memoir Institute of Geological Services, no. RP10, 369 p.

Crow, M.J., and Zaw, K., 2017, Geochronology in Myanmar (1964–2017): Geological Society of London Memoirs, v. 48, no. 1, p. 713–759.

Cumming, G.V., James, R., Salam, A., Zaw, K., Meffre, S., Lunwongsa, W., and Nuanla-ong, S., 2008, Geology and mineralization of the Chatree epithermal gold-silver deposit, Phetchabun Province, central Thailand: Australasian Institute of Mining and Metallurgy (AusIMM) PACRIM Congress, Australia, 2008, Proceedings, p. 409–416.

Dew, R.E.C., Collins, A.S., Glorie, S., Morley, C.K., Blades, M.L., Nachtergaele, S., King, R., Foden, J., De Grave, J., Kanjanapayont, P., Evans, N.J., Alessio, B.L., and Charusiri, P., 2018, Probing into Thailand's basement: New insights from U-Pb geochronology, Sr, Sm-Nd, Pb and Lu-Hf isotopic systems from granitoids: Lithos, v. 320–321, p. 332–354.

Dong, M.L., Dong, G.C., Mo, X.X., Zhu, D.C., Nie, F., Yu, J.C., Wang, P., and Luo, W., 2013, The Mesozoic-Cenozoic magmatism in Baoshan block, western Yunnan and its tectonic significance: Acta Petrologica Sinica, v. 29, no. 11, p. 3901–3913 (in Chinese with English abs.).

Du, A.D., Wu, S.Q., Sun, D.Z., Wang, S.X., Qu, W.J., Markey, R., Stain, H., Morgan, J., and Malinovskiy, D., 2004, Preparation and certification of Re-Os dating reference materials: Molybdenites HLP and JDC: Geostandards and Geoanalytical Research, v. 28, no. 1, p. 41–52.

Fanka, A., Tsunogae, T., Daorerk, V., Tsutsumi, Y., Takamura, Y., and Sutthirat, C., 2018, Petrochemistry and zircon U-Pb geochronology of granitic rocks in the Wang Nam Khiao area, Nakhon Ratchasima, Thailand: Implications for petrogenesis and tectonic setting: Journal of Asian Earth Sciences, v. 157, p. 92–118.

Farmer, C.B., Searl, A., and Halls, C., 1991, Cathodoluminescence and growth of cassiterite in the composite lodes at South Crofty mine, Cornwall, England: Mineralogical Magazine, v. 55, p. 447–458.

Fournier, R.O., 1999, Hydrothermal processes related to movement of fluid from plastic into brittle rock in the magmatic-epithermal environment: Economic Geology, v. 94, p. 1193–1211.

Gardiner, N.J., Robb, L.J., and Searle, M.P., 2014, The metallogenic provinces of Myanmar: Applied Earth Science, v. 123, p. 25–38.

Gardiner, N.J., Searle, M.P., Robb, L.J., and Morley, C.K., 2015a, Neo-Tethyan magmatism and metallogeny in Myanmar—an Andean analogue?: Journal of Asian Earth Sciences, v. 106, p. 197–215.

Gardiner, N.J., Sykes, J.P., Trench, A., and Robb, L.J., 2015b, Tin mining in Myanmar: Production and potential: Resources Policy, v. 46, p. 219–33.

Gardiner, N.J., Robb, L.J., Morley, C.K., Searle, M.P., Cawood, P.A., Whitehouse, M.J., Kirkland, C.L., Roberts, N.M.W., and Myint, T.A., 2016a, The tectonic and metallogenic framework of Myanmar: A Tethyan mineral system: Ore Geology Reviews, v. 79, p. 26–45.

Gardiner, N.J., Searle, M.P., Morley, C.K., Whitehouse, M.P., Spencer, C.J., and Robb, L.J., 2016b, The closure of Palaeo-Tethys in eastern Myanmar and northern Thailand: New insights from zircon U-Pb and Hf isotope data: Gondwana Research, v. 39, p. 401–422.

Gardiner, N.J., Hawkesworth, C.J., Robb, L.J., Whitehouse, M.J., Roberts, N.M., Kirkland, C.L., and Evans, N.J., 2017, Contrasting granite metallogeny through the zircon record: A case study from Myanmar: Scientific Reports, v. 7, no. 1, p. 748.

Gardiner, N.J., Searle, M.P., Morley, C.K., Robb, L.J., Whitehouse, M.J., Roberts, N.M.W., Kirkland, C.L., and Spencer, C.J., 2018, The crustal architecture of Myanmar imaged through zircon U-Pb, Lu-Hf and O isotopes: Tectonic and metallogenic implications: Gondwana Research, v. 62, p. 27–60.

Giles, D.L., and Shilling, J.H., 1972, Variation in rhenium content of molybdenite: International Geological Congress Section, 24th, Montreal, Quebec, Canada, August 21–29, 1972, Proceedings, p. 145–152.

Griffin, W.L., Wang, X., Jackson, S.E., Pearson, N.J., O'Reilly, S.Y., Xu, X.S., and Zhou, X.M., 2002, Zircon chemistry and magma mixing, SE China: In-situ analysis of Hf isotopes, Tonglu and Pingtan igneous complexes: Lithos, v. 61, p. 237–269.

Gulson, B.L., and Jones, M.T., 1992, Cassiterite—potential for direct dating of mineral-deposits and a precise age for the Bushveld Complex granites: Geology, v. 20, p. 355–358.

Hanchar, J.M., and Hoskin, P.W.O., 2003, Zircon: Reviews in Mineralogy and Geochemistry, v. 53, 500 p.

Heinrich, C.A., 1990, The chemistry of hydrothermal tin(-tungsten) ore deposition: Economic Geology, v. 85, p. 457–481.

Heinrich, C.A., Halter, W., Landtwing, M.R., and Pettke, T., 2005, The formation of economic porphyry copper (-gold) deposits: Constraints from microanalysis of fluid and melt inclusions: Geological Society of London, Special Publication 248, p. 247–263.

Henley, R.W., King, P.L., Wykes, J.L., Renggli, C.J., Brink, F.J., Clark, D.A., and Troitzsch, U., 2015, Porphyry copper deposit formation by sub-volcanic sulphur dioxide flux and chemisorption: Nature Geoscience, v. 8, p. 210–215.

Hou, Z., and Zhang, H., 2015, Geodynamics and metallogeny of the eastern Tethyan metallogenic domain: Ore Geology Reviews, v. 70, p. 346–384.

Htun, T., Htay, T., and Zaw, K., 2017, Tin-tungsten deposits of Myanmar: Geological Society of London Memoirs, v. 48, p. 625–647.

Hutchison, C.S., 1975, Ophiolite in Southeast Asia: Geological Society of America Bulletin, v. 86, p. 797–806.

——1977, Granite emplacement and tectonic subdivision in Peninsular Malaysia: Bulletin of the Geological Society of Malaysia, v. 9, p. 187–207.

——1983, Multiple Mesozoic Sn-W-Sb granitoids of Southeast Asia: Geological Society of America Memoirs, v. 159, p. 35–60.

——1994, Gondwana and Cathaysian blocks, Palaeotethys sutures and Cenozoic tectonics in South-east Asia: Geologische Rundschau, v. 83, p. 388–405.

Hutchison, C.S., and Taylor, D., 1978, Metallogenesis in SE Asia: Journal of the Geological Society, London, v. 35, p. 407–428.

Jiang, H., Li, W.Q., Jiang, S.Y., Wang, H., and Wei, X.P., 2017, Geochronological, geochemical and Sr-Nd-Hf isotopic constraints on the petrogenesis of Late Cretaceous A-type granites from the Sibumasu block, southern Myanmar, SE Asia: Lithos, v. 268, p. 32–47.

Jiang, S.Y., Yu, J.M., and Lu, J.J., 2004, Trace and rare-earth element geochemistry in tourmaline and cassiterite from the Yunlong tin deposit, Yunnan, China: Implication for migmatitic-hydrothermal fluid evolution and ore genesis: Chemical Geology, v. 209, p. 193–213.

Kettle, P., Pearce, J., Lin, C., and Sykes, J.P., 2014, Tin industry review: Managing the next tin crisis: International Tin Research Institute, Ltd., St. Albans, United Kingdom, Online Press Release, www.internationaltin.org.

Kettle, P., Lin, C., Tianhua, R., Mulqueen, T., and Davidson, V., 2015, CRUMonitor tin: Tin market lacking direction as trading slows: CRU Group Ltd. in association with International Tin Research Institute, Ltd., St. Albans, United Kingdom, Online Press Release, June 11, 2015, www.internationaltin.org.

Khositanont, S., 1990, The genesis of the Sn-W deposits at Samoeng mine, Thailand: Evidence from fluid inclusions: Ph.D. thesis, Quebec, Canada, University of Quebec, 124 p.

Kinny, P.D., and Maas, R., 2003, Lu-Hf and Sm-Nd isotope systems in zircon: Reviews in Mineralogy and Geochemistry, v. 53, p. 327–341.

Lehmann, B., 1990, Model of tin ore formation, *in* Metallogeny of tin: Lecture notes in earth sciences, v. 32, Berlin, Heidelberg, Springer, p. 146–177.

Lehmann, B., and Mahawat, C., 1989, Metallogeny of tin in central Thailand—a genetic concept: Geology, v. 17, p. 426–429.

Leong, K.S., 1985, Geology, mineralisation and soil geochemical studies of the Kroh-Khan Intan area, Upper Perak: B.Sc. thesis, Kuala Lumpur, University of Malaya, 67 p.

Li, C.Y., Zhang, R.Q., Ding, X., Ling, M.X., Fan, W.M., and Sun, W.D., 2016, Dating cassiterite using laser ablation ICP-MS: Ore Geology Reviews, v. 72, p. 313–322.

Li, D.P., Chen, Y.L., Hou, K.J., and Luo, Z.H., 2016, Origin and evolution of the Tengchong block, southeastern margin of the Tibetan Plateau: Zircon U-Pb and Lu-Hf isotopic evidence from the (meta-) sedimentary rocks and intrusions: Tectonophysics, v. 687, p. 245–256.

Li, H., Myint, A.Z., Yonezu, K., Watanabe, K., Algeo, T.J., and Wu, J.H., 2018, Geochemistry and U-Pb geochronology of the Wagone and Hermyingyi A-type granites, southern Myanmar: Implications for tectonic setting, magma evolution and Sn-W mineralization: Ore Geology Reviews, v. 95, p. 575–592.

Li, J., Zhong, L.F., Tu, X.L., Liang, X.R., and Xu, J.F., 2010, Determination of rhenium content in molybdenite by ICP-MS after separation of the major matrix by solvent extraction with N-benzoyl-N-phenylhydroxalamine: Talanta, v. 81, p. 954–958.

Li, J.X., Zhang, L.Y., Fan, W.M., Ding, L., Sun, Y.L., Peng, T.P., Li, G.M., and Sein, K., 2018, Mesozoic-Cenozoic tectonic evolution and metallogeny in Myanmar: Evidence from zircon/cassiterite U-Pb and molybdenite Re-Os geochronology: Ore Geology Reviews, v. 102, p. 829–845.

Li, X.H., Long, W.G., Li, Q.L., Liu, Y., Zheng, Y.F., Yang, Y.H., Chamberlain, K.R., Wan, D.F., Guo, C.H., Wang, X.C., and Tao, H., 2010, Penglai zircon megacrysts: A potential new working reference material for microbeam determination of Hf-O isotopes and U-Pb ages: Geostandards and Geoanalytical Research, v. 34, p. 117–134.

Lin, T.H., Mitchell, A.H.G., Chung, S.L., Tan, X.B., Tang, J.T., Oo, T., and Wu, F.Y., 2019, Two parallel magmatic belts with contrasting isotopic characteristics from southern Tibet to Myanmar: Zircon U-Pb and Hf isotopic constraints: Journal of the Geological Society, London, v. 176, p. 574–587.

Linnen, R.L., and Williams-Jones, A.E., 1995, Genesis of a magmatic metamorphic hydrothermal system: The Sn-W polymetallic deposits at Pilok, Thailand: Economic Geology, v. 90, p. 1148–1166.

Liu, C.Z., Chung, S.L., Wu, F.Y., Zhang, C., Xu, Y., Wang, J.G., Chen, Y., and Guo, S., 2016a, Tethyan suturing in Southeast Asia: Zircon U-Pb and Hf-O isotopic constraints from Myanmar ophiolites: Geology, v. 44, p. 311–314.

Liu, C.Z., Zhang, C., Xu, Y., Wang, J.G., Chen, Y., Guo, S., Wu, F.Y., and Sein, K., 2016b, Petrology and geochemistry of mantle peridotites from the Kalaymyo and Myitkyina ophiolites (Myanmar): Implications for tectonic settings: Lithos, v. 264, p. 495–508.

Liu, Y.S., Hu, Z.C., Gao, S., Güther, D., Xu, J., Gao, C.G., and Chen, H.H., 2008, In situ analysis of major and trace elements of anhydrous minerals by LA-ICP-MS without applying an internal standard: Chemical Geology, v. 257, no. 1–2, p. 34–43.

Liu, Y.S., Hu, Z.C., Zong, K.Q., Gao, C.G., Gao, S., Xu, J., and Chen, H.H., 2010, Reappraisement and refinement of zircon U-Pb isotope and trace element analyses by LA-ICP-MS: Chinese Science Bulletin, v. 55, no. 15, p. 1535–1546.

Ludwig, K.R., 2003, User's manual for Isoplot/Ex., version 3.00: A geochronological toolkit for Microsoft Excel: Berkeley, California, Berkeley Geochronology Center Special Publication, p. 1–70.

Manning, D.A.C., 1986, Contrasting styles of Sn-W mineralization in peninsular Thailand and SW England: Mineralium Deposita, v. 21, p. 44–52.

Mao, J., Zhang, Z., Zhang, Z., and Du, A., 1999, Re-Os isotopic dating of molybdenites in the Xiaoliugou W (Mo) deposit in the northern Qilian mountains and its geological significance: Geochimica et Cosmochimica Acta, v. 63, p. 1815–1818.

Mao, W., Rusk, B., Yang, F., and Zhang, M., 2017, Physical and chemical evolution of the Dabaoshan porphyry Mo deposit, South China: Insights from fluid inclusions, cathodoluminescence, and trace elements in quartz: Economic Geology, v. 112, p. 889–918.

Mao, W., Zhong, H., Zhu, W.G., Lin, X.G., and Zhao, X.Y., 2018, Magmatic-hydrothermal evolution of the Yuanzhuding porphyry Cu-Mo deposit, South China: Insights from mica and quartz geochemistry: Ore Geology Reviews, v. 101, p. 765–784.

Mattinson, J.M., 1987, U-Pb ages of zircons: A basic examination of error propagation: Chemical Geology, v. 66, p. 151–162.

Mercer, C.N., Reed, M.H., and Mercer, C.M., 2015, Time scales of porphyry Cu deposit formation: Insights from titanium diffusion in quartz: Economic Geology, v. 110, p. 587–602.

Metcalfe, I., 1984, Stratigraphy, palaeontology and palaeogeography of the Carboniferous of Southeast Asia: Memoires de la Societe Geographique de France, v. 147, p. 107–118.

——1988, Origin and assembly of south-east Asian continental terranes: Geological Society of London, Special Publication 37, p. 101–118.

——1996, Pre-Cretaceous evolution of SE Asian terranes: Geological Society of London, Special Publication 106, p. 97–122.

——1998, Palaeozoic and Mesozoic geological evolution of the SE Asian region: Multidisciplinary constraints and implications for biogeography, *in* Hall, R., and Holloway, J.D., eds., Biogeography and geological evolution of SE Asia: Leiden, The Netherlands, Backhuys Publishers, p. 25–41.

——2009, Late Palaeozoic and Mesozoic tectonic and palaeogeographical evolution of SE Asia: Geological Society of London, Special Publication 315, p. 7–23.

——2011, Palaeozoic-Mesozoic history of SE Asia: Geological Society of London, Special Publication 355, p. 7–35.

——2013, Gondwana dispersion and Asian accretion: Tectonic and palaeogeographic evolution of eastern Tethys: Journal of Asian Earth Sciences, v. 66, p. 1–33.

Mitchell, A.H.G., 1977, Tectonic settings for the emplacement of Southeast Asian tin granites: Bulletin of the Geological Society of Malaysia, v. 9, p. 123–140.

——1979, Rift-, subduction- and collision-related tin belts: Bulletin of the Geological Society of Malaysia, v. 11, p. 81–102.

——1981, Phanerozoic plate boundaries in mainland SE Asia, the Himalayas and Tibet: Journal of the Geological Society, London, v. 138, p. 109–122.

——1986, Mesozoic and Cenozoic regional tectonics and metallogenesis in Mainland SE Asia: Bulletin of the Geological Society of Malaysia, v. 20, p. 221–239.

——1992, Late Permian-Mesozoic events and the Mergui Group nappe in Myanmar and Thailand: Journal of Southeast Asian Earth Sciences, v. 7, p. 165–178.

——1993, Cretaceous-Cenozoic tectonic events in the western Myanmar (Burma)-Assam region: Journal of the Geological Society, London, v. 150, p. 1809–1102.

——2018, Geological belts, plate boundaries, and mineral deposits in Myanmar: Amsterdam, Elsevier, 509 p.

Mitchell, A.H.G., and Garson, M.S., 1981, Mineral deposits and global tectonic settings: New York, Academic Press, 405 p.

Mitchell, A.H.G., Myint, W., Lynn, K., Htay, M.T., Oo, M., and Zaw, T., 2011, Geology of the high sulfidation copper deposits, Monywa mine, Myanmar: Resource Geology, v. 61, p. 1–29.

Mitchell, A.H.G., Chung, S.L., Oo, T., Lin, T.H., and Hung, C.H., 2012, Zircon U-Pb ages in Myanmar: Magmatic-metamorphic events and the closure of a Neo-Tethys Ocean?: Journal of Asian Earth Sciences, v. 56, p. 1–23.

Mitchell, A.H.G., Htay, M.T., and Htun, K.M., 2015, The medial Myanmar suture zone and the Western Myanmar-Mogok foreland: Journal of Myanmar Geosciences Society, v. 6, p. 73–88.

Möller, P., Dulski, P., Szacki, W., Malow, G., and Riedel, E., 1988, Substitution of tin in cassiterite by tantalum, niobium, tungsten, iron and manganese: Geochimica et Cosmochimica Acta, v. 52, p. 1497–1503.

Murciego, A., Sanchez, A.G., Dusausoy, Y., Pozas, J.M.M., and Ruck, R., 1997, Geochemistry and EPR of cassiterites from the Iberian Hercynian massif: Mineralogical Magazine, v. 61, p. 357–365.

Myanmar Geosciences Society, 2014, Geological map of Myanmar: Yangon, Myanmar, scale 1:2,250,000.

Myint, A.Z., Yonezu, K., Boyce, A.J., Selby, D., Scherstén, A., Tindell, T., Watanabe, K., and Swe, Y.M., 2018, Stable isotope and geochronological study of the Mawchi Sn-W deposit, Myanmar: Implications for timing of mineralization and ore genesis: Ore Geology Reviews, v. 95, p. 663–679.

Myint, K.K., 1994, Mineral belts and epochs in Myanmar: Resource Geology, v. 44, p. 231–240.

Neiva, A.M.R., 2008, Geochemistry of cassiterite and wolframite from tin and tungsten quartz veins in Portugal: Ore Geology Reviews, v. 33, p. 221–238.

Ng, S.W.P., Chung, S.L., Robb, L.J., Searle, M.P., Ghani, A.A., Whitehouse, M.J., Oliver, G.J.H., Sone, M., Gardiner, N.J., and Roselee, M.H., 2015a, Petrogenesis of Malaysian granitoids in the Southeast Asian tin belt: Part 1. Geochemical and Sr-Nd isotopic characteristics: Geological Society of America Bulletin, v. 127, p. 1209–1237.

Ng, S.W.P., Whitehouse, M.J., Searle, M.P., Robb, L.J., Ghani, A.A., Chung, S.L., Oliver, G.J.H., Sone, M., Gardiner, N.J., and Roselee, M.H., 2015b, Petrogenesis of Malaysian granitoids in the Southeast Asian tin belt: Part 2. U-Pb zircon geochronology and tectonic model: Geological Society of America Bulletin, v. 127, p. 1238–1258.

Oldham, T., 1856, Notes on the coal field and tin-stone deposits of the Tenasserim provinces: Selected Records in Geology, Government of India, v. 10, p. 31–67.

Parafiniuk, J., Gołębiowska, B., and Pieczka, A., 2007, Geochemistry and origin of the cassiterite from Rędziny, Lower Silesia, Poland: Mineralogia, v. 38, p. 219–230.

Pašava, J., Svojtk, M., Veselovský, F., Ďurišová, J., Ackerman, L., Pour, O., Drábek, M., Halodová, P., and Haluzová, E., 2016, Laser ablation ICPMS study of trace element chemistry in molybdenite coupled with scanning electron microscopy (SEM)—an important tool for identification of different types of mineralization: Ore Geology Reviews, v. 72, p. 874–895.

Pavlova, G.G., Palessky, S.V., Borisenko, A.S., Vladimirov, A.G., Seifert, T., and Phan, L.A., 2015, Indium in cassiterite and ores of tin deposits: Ore Geology Reviews, v. 66, p. 99–113.

Penzer, N.M., 1922, The mineral resources of Burma: London, George Routledge and Sons, p. 1–177.

Plimer, I.R., Lu, J., and Kleeman, J.D., 1991, Trace and rare earth elements in cassiterite—sources of components for the tin deposits of the Mole granite, Australia: Mineralium Deposita, v. 26, p. 267–274.

Pollard, P.J., Nakapadungrat, S., and Taylor, R.G., 1995, The Phuket Supersuite, southwest Thailand: Fractionated I-type granites associated with tin-tantalum mineralization: Economic Geology, v. 90, p. 586–602.

Putthapiban, P., and Gray, D., 1983, Age and tin-tungsten mineralization of the Phuket granites, Thailand: Geology and Mineral Resources of Thailand Conference, Department of Mineral Resources, Bangkok, 1983, Proceedings, p. 10.

Qi, L., Zhou, M.F., Gao, J., and Zhao, Z., 2010, An improved Carius tube technique for determination of low concentrations of Re and Os in pyrites: Journal of Analytical Atomic Spectrometry, v. 25, p. 585–589.

Rathkopf, C., Mazdab, F., Barton, I., and Barton, M.D., 2017, Grain-scale and deposit-scale heterogeneity of Re distribution in molybdenite at the Bagdad porphyry Cu-Mo deposit, Arizona: Journal of Geochemical Exploration, v. 178, p. 45–54.

Remond, G., 1973, Exemples d'identification et de localisation des elements en trace dans les mineraux luminescents a l'aide de la microsonde ionique: Bulletin de la Société française de Minéralogie et de Cristallographie, v. 96, p. 183–198.

Romer, R.L., Thomas, R., Stein, H.J., and Rhede, D., 2007, Dating multiply overprinted Sn-mineralized granites—an example from the Erzgebirge, Germany: Mineralium Deposita, v. 42, p. 337–359.

Rusk, B., and Reed, M., 2002, Scanning electron microscope-cathodoluminescence analysis of quartz reveals complex growth histories in veins from the Butte porphyry copper deposit, Montana: Geology, v. 30, p. 727–730.

Rusk, B.G., 2012, Cathodoluminescent textures and trace elements in hydrothermal quartz, in Gotze, J., and Mockel, R., eds., Quartz: Deposits, mineralogy and analytics, 1st ed.: Springer Geology, p. 307–329.

Salam, A., Zaw, K., Meffre, S., McPhie, J., and Lai, C.K., 2014, Geochemistry and geochronology of the Chatree epithermal gold-silver deposit: Implications for the tectonic setting of the Loei fold belt, central Thailand: Gondwana Research, v. 26, p. 198–217.

Sanematsu, K., Manaka, T., and Zaw, K., 2014, Geochemical and geochronological characteristics of granites and Sn-W-REE mineralisation in the Thanintharyi region, southern Myanmar: GEOSEA XIII—GEOMYANMAR 2014, 13th Regional Congress on Regional Geology, Mineral and Energy Resources of Southeast Asia, Myanmar Geosciences Society, Yangon, 2014, Abstracts, p. 19–20.

Scherer, E., Münker, C., and Mezger, K., 2001, Calibration of the lutetium-hafnium clock: Science, v. 293, p. 683–687.

Schwartz, M.O., Rajah, S.S., Askury, A.K., Phutthapiban, P., and Djaswadi, S., 1995, The Southeast Asian tin belt: Earth-Science Reviews, v. 38, p. 95–293.

Searle, M.P., Noble, S.R., Cottle, J.M., Waters, D.J., Mitchell, A.H.G., Hlaing, T., and Horstwood, M.S.A., 2007, Tectonic evolution of the Mogok metamorphic belt, Burma (Myanmar) constrained by U-Th-Pb dating of metamorphic and magmatic rocks: Tectonics, v. 26, doi: 10.1029/2006TC002083.

Searle, M.P., Whitehouse, M.J., Robb, L.J., Ghani, A.A., Hutchison, C.S., Sone, M., Ng, S.W.P., Hatta, M., Chung, S.L., and Oliver, G.J.H., 2012, Tectonic evolution of the Sibumasu-Indochina terrane collision zone in Thailand and Malaysia—constraints from new U-Pb zircon chronology of SE Asian granitoids: Journal of the Geological Society, London, v. 169, p. 489–500.

Selby, D., and Creaser, R.A., 2004, Macroscale NTIMS and microscale LA-MC-ICP-MS Re-Os isotopic analysis of molybdenite: Testing restrictions for reliable Re-Os age determinations, and implications for the decoupling of Re and Os within molybdenite: Geochimica et Cosmochimica Acta, v. 68, p. 3897–3908.

Sengor, A.M.C., 1979, Mid-Mesozoic closure of Permo-Triassic Tethys and its implications: Nature, v. 279, p. 590–593.

——1984, The Cimmeride orogenic system and the tectonics of Eurasia: Geological Society of America, Special Paper 195, p. 1–82.

——1987, Tectonics of the Tethysides: Orogenic collage development in a collisional setting: Annual Review of Earth and Planetary Sciences, v. 15, p. 213–244.

Shawe, D.R., 1984, Geology and mineral deposits of Thailand: U.S. Geological Survey, Open-File Report 84-403, 195 p.

Shinotsuka, K., and Suzuki, K., 2007, Simultaneous determination of platinum group elements and rhenium in rock samples using isotope dilution inductively coupled plasma mass spectrometry after cation exchange separation followed by solvent extraction: Analytica Chimica Acta, v. 603, p. 129–139.

Shirey, S.B., and Walker, R.J., 1998, The Re-Os isotope system in cosmochemistry and high temperature geochemistry: Annual Review of Earth and Planetary Sciences, v. 26, p. 423–500.

Sinclair, D.W., Jonasson, I.R., Kirkham, R.V., and Soregaroli, A.E., 2009, Rhenium and other platinum-group metals in porphyry deposits: Geological Survey of Canada, Open File 6181, 1 sheet.

Sippel, R.F., 1968, Sandstone petrology, evidence from luminescence petrography: Journal of Sedimentary Research, v. 38, p. 530–554.

Sláma, J., Košler, J., Condon, D.J., Crowley, J.L., Gerdes, A., Hanchar, J.M., Horstwood, M.S.A., Morris, G.A., Nasdala, L., Norberg, N., Schaltegger, U., Schoene, B., Tubrett, M.N., and Whitehouse, M.J., 2008, Plešovice zircon—a new natural reference material for U-Pb and Hf isotopic microanalysis: Chemical Geology, v. 249, p. 1–35.

Smith, J.V., and Stenstrom, R.C., 1965, Electron-excited luminescence as a petrologic tool: The Journal of Geology, v. 73, p. 627–635.

Smoliar, M.I., Walker, R.J., and Morgan, J.W., 1996, Re-Os ages of group IIA, IIIA, IVA, and IVB iron meteorites: Science, v. 271, p. 1099–1102.

Sone, M., and Metcalfe, I., 2008, Parallel Tethyan sutures in mainland SE Asia: New insights for Palaeo-Tethys closure: Compte Rendus Geoscience, v. 340, p. 166–179.

Stein, H.J., Markey, R.J., Morgan, J.W., Hannah, J.L., and Schersten, A., 2001, The remarkable Re-Os chronometer in molybdenite: How and why it works: Terra Nova, v. 13, p. 479–486.

Stein, H.J., Schersten, A., Hannah, J.L., and Markey, R.J., 2003, Subgrain decoupling of Re and [187]Os and assessment of laser ablation ICP-MS spot dating in molybdenite: Geochimica et Cosmochimica Acta., v. 67, p. 3673–3686.

Thein, M., 2017, Current tectonic activity along the Sagaing fault, Myanmar indicated by alluvial fans: Geological Society, London, Memoirs, v. 48, p. 443–452.

Tindle, A.G., and Breaks, F.W., 1998, Oxide minerals of the Separation Rapids rare-element granitic pegmatite group, northwestern Ontario: The Canadian Mineralogist, v. 36, p. 609–635.

Vervoort, J.D., Patchett, P.J., Soderlund, U., and Baker, M., 2004, Isotopic composition of Yb and the determination of Lu concentrations and Lu/Hf by isotope dilution using MC-ICPMS: Geochemistry Geophysics Geosystems, v. 5, p. 1–15.

Voudouris, P.C., Melfos, V., Spry, P.G., Bindi, L., Kartal, T., Arikas, K., Moritz, R., and Ortelli, M., 2009, Rhenium-rich molybdenite and rheniite in the Pagoni Rachi Mo-Cu-Te-Ag-Au prospect, northern Greece: Implications for the Re geochemistry of porphyry style Cu-Mo and Mo mineralization: The Canadian Mineralogist, v. 47, p. 1013–1036.

Wang, B.D., Wang, L.Q., Chung, S.L., Chen, J.L., Yin, F.G., Liu, H., Li, X.B., and Chen, L.K., 2016, Evolution of the Bangong-Nujiang Tethyan Ocean: Insights from the geochronology and geochemistry of mafic rocks within ophiolites: Lithos, v. 245, p. 18–33.

Wang, C., Deng, J., Carranza, E.J.M., and Santosh, M., 2014, Tin metallogenesis associated with granitoids in the southwestern Sanjiang Tethyan domain: Nature, deposit types, and tectonic setting: Gondwana Research, v. 26, p. 576–593.

Wang, Y., Qian, X., Cawood, P.A., Liu, H., Feng, Q., Zhao, G., Zhang, Y., He, H., and Zhang, P., 2018, Closure of the East Paleotethyan Ocean and amalgamation of the Eastern Cimmerian and Southeast Asia continental fragments: Earth-Science Reviews, p. 186, v. 195–230.

Wiedenbeck, M., Allé, P., Corfu, F., Griffin, W.L., Meier, M., Oberli, F., von Quadt, A., Roddick, J.C., and Spiegel, W., 1995, Three natural zircon standards for U-Th-Pb, Lu-Hf, trace element and REE analyses: Geostandards Newsletter, v. 19, p. 1–23.

Win, S., and Myint, M.M., 1998, Mineral potential of Myanmar: Resource Geology, v. 48, p. 209–218.

Wopfner, H., 1996, Gondwana origin of the Baoshan and Tengchong terranes of west Yunnan: Geological Society of London, Special Publication 106, p. 539–547.

Wu, F.Y., Yang, Y.H., Xie, L.W., Yang, J.H. and Xu, P., 2006, Hf isotopic compositions of the standard zircons and baddeleyites used in U-Pb geochronology: Chemical Geology, v. 234, p. 105–126.

Xie, J.C., Zhu, D.C., Dong, G., Zhao, Z.D., Wang, Q., and Mo, X., 2016, Linking the Tengchong terrane in SW Yunnan with the Lhasa terrane in southern Tibet through magmatic correlation: Gondwana Research, v. 39, p. 217–229.

Xu, Y.G., Yang, Q.J., Lan, J.B., Luo, Z.Y., Huang, X.L., Shi, Y.R., and Xie, L.W., 2012, Temporal-spatial distribution and tectonic implications of the batholiths in the Gaoligong-Tengliang-Yingjiang area, western Yunnan: Constraints from zircon U-Pb ages and Hf isotopes: Journal of Asian Earth Sciences, v. 53, p. 151–175.

Yeap, E.B.,1978, Hydrothermal tin-bearing breccias of the Yap Peng mine, Sungai Besi, Selangor, Peninsular Malaysia: Regional Conference on Geology and Mineral Resources of Southeast Asia, 3rd, Bangkok, November 14–18, 1978, Proceedings, p. 367–375.

——1993, Tin and gold mineralizations in Peninsular Malaysia and their relationships to the tectonic development: Journal of Southeast Asian Earth Sciences, v. 8, p. 329–348.

Yu, L., Li, G.J., Wang, Q.F., and Liu, X.F., 2014, Petrogenesis and tectonic significance of the Late Cretaceous magmatism in the northern part of the Baoshan block: Constraints from bulk geochemistry, zircon U-Pb geochronology and Hf isotope compositions: Acta Petrologica Sinica, v. 30, p. 2709–2724 (in Chinese with English abs.).

Yuan, S.D., Peng, J.T., Hao, S., Li, H.M., Geng, J.Z., and Zhang, D.L., 2008, A precise U-Pb age on cassiterite from the Xianghualing tin-polymetallic deposit (Hunan, South China): Mineralium Deposita, v. 43, p. 375–382.

Yuan, S.D., Peng, J.T., Hu, R.Z., Li, H.M., Shen, N.P., and Zhang, D.L., 2011, In situ LA-MC-ICP-MS and ID-TIMS U-Pb geochronology of cassiterite in the giant Furong tin deposit, Hunan Province, South China: New constraints on the timing of tin-polymetallic mineralization: Ore Geology Reviews, v. 43, p. 235–242.

Zaw, K., 1984, Geology and geothermometry of vein-type W-Sn deposits at Pennaichaung and Yetkanzintaung prospects, Tavoy Township, Tennasserim division, southern Burma: Mineralium Deposita, v. 19, p. 138–144.

——1990, Geological, petrological and geochemical characteristics of granitoid rocks in Burma—with special reference to the associated W-Sn mineralization and their tectonic setting: Journal of Southeast Asian Earth Sciences, v. 4, p. 293–335.

——2017, Overview of mineralization styles and tectonic-metallogenic setting in Myanmar: Geological Society, London, Memoirs, v. 48, p. 531–556.

Zaw, K., Meffre, S., Lai, C.-K., Burrett, C., Santosh, M., Graham, I., Manaka, T., Salam, A., Kamvong, T., and Cromie, P., 2014, Tectonics and metallogeny of mainland Southeast Asia—a review and contribution: Gondwana Research, v. 26, p. 5–30.

Zaw, K., Win, S., Barber, A.J., Crow, M.J., and Yin Yin, N., 2017, Myanmar: Geology, resources, and tectonics: Geological Society, London, Memoirs, v. 48, 759 p.

Zhang, R., Lehmann, B., Seltmann, R., Sun, W., and Li, C., 2017a, Cassiterite U-Pb geochronology constrains magmatic-hydrothermal evolution in complex evolved granite systems: The classic Erzgebirge tin province (Saxony and Bohemia): Geology, v. 45, p. 1095–1098.

Zhang, R., Lu, J., Lehmann, B., Li, C., Li, G., Zhang, L., Guo, J., and Sun, W., 2017b, Combined zircon and cassiterite U-Pb dating of the Piaotang granite-related tungsten-tin deposit, southern Jiangxi tungsten district, China: Ore Geology Reviews, v. 82, p. 268–284.

Zhang, Z., Shu, Q., Yang, X., Wu, C., Zheng, C., and Xu, J., 2019, Review on the tectonic terranes associated with metallogenic zones in Southeast Asia: Journal of Earth Science, v. 30, p. 1–19.

Zhirov, K.K., and Ivanova, G.F., 1959, The distribution of rhenium in molybdenites of deposits of various genetic types: Geokhimiya, v. 6, p. 518–523.

Zhou, X.P., Qi, H.W., Qu, W.J., and Li, C., 2017, Re-Os isotopic dating for molybdenites in Xinqi tungsten-tin polymetallic deposit of Yunnan Province, China and its geological significance: Acta Mineralogica Sinica, v. 37, p. 84–92 (in Chinese with English abs.).

Wei Mao is currently a postdoctoral researcher at the Institute of Geochemistry, Chinese Academy of Sciences. He gained his B.S. degree in geology from Northwest University, Xi'an, China, in 2011 and a Ph.D. degree in economic geology from the University of Chinese Academy of Sciences in 2016. He worked with Brian Rusk from April 2014 to February 2015 at the Western Washington University, United States, as a joint-training Ph.D. student. His research interest focuses on ore-forming mechanisms of magmatic-hydrothermal deposits. He mainly works on porphyry Cu-Mo deposits in south China and granite-related Sn-W deposits in Southeast Asia.